CHALMERS

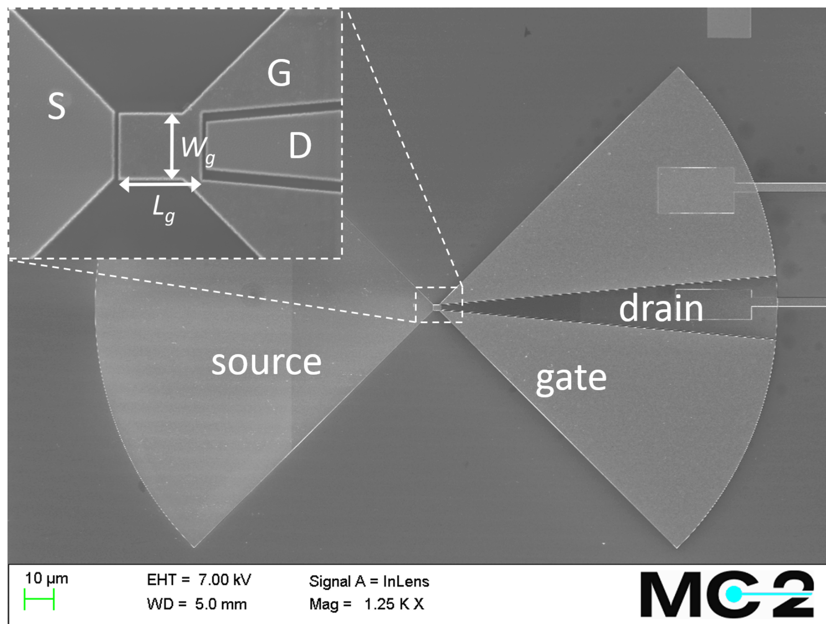

Bow-tie antenna-coupled graphene FETs for direct detection at 0.6 THz

Thesis for Erasmus Mundus Master of Science in Nanoscience and Nanotechnology

AUDREY ZAK

Department Microtechnology and Nanoscience
Terahertz and Millimetre Wave Laboratory
CHALMERS UNIVERSITY OF TECHNOLOGY
Gothenburg, Sweden 2014

Education and Culture
Erasmus Mundus

KU LEUVEN

Thesis for the degree of

Erasmus Mundus Master of Nanoscience and Nanotechnology in Nanoelectronics

Bow-tie antenna-coupled graphene FETs for direct detection at 0.6 THz

Audrey Zak

Promoter

Prof. Jan Stake, Chalmers

Co-promoter

Prof. Marc Heyns, KU Leuven

Supervisor

Michael Andersson

Terahertz and Millimetre Wave Laboratory
Department of Microtechnology and Nanoscience
Chalmers University of Technology
Göteborg, Sweden 2014

CHALMERS

Education and Culture

Erasmus Mundus

KU LEUVEN

Bow-tie antenna-coupled graphene FETs for direct detection at 0.6 THz
Audrey Zak

©Audrey Zak, 2014
Chalmers University of Technology
Department of Microtechnology and Nanoscience
Terahertz and Millimetre Wave Laboratory
SE-412 96 Göteborg, Sweden
Phone: +46 (0) 31 772 1000

Cover: SEM image of a split bow-tie antenna-integrated GFET with inset highlighting important transistor dimensions. Inset scale bar is 2 μm.

Printed by Chalmers Reproservice
Göteborg, Sweden 2014

To my family

Abstract

The recent demonstration of the electric field effect in graphene, a two-dimensional carbon lattice, and the measurement of its extraordinary room-temperature properties have sparked enormous interest in graphene as a material in electronics. Atomically thin and conductive, graphene has many options for integration with existing electronic devices and opportunities for the development of new devices. Graphene has a high carrier mobility and high carrier saturation velocity at room temperature, two properties which give it the potential for use in high-speed, high-frequency applications. Technologies operating at terahertz (1×10^{12} Hz) frequencies are becoming more numerous as an effort is made to close the so-called *terahertz gap*, and graphene has recently emerged as a viable terahertz material.

This thesis presents terahertz (THz) direct detectors based on antenna-coupled graphene field effect transistors (GFETs). These GFETs were fabricated using both mechanically exfoliated graphene and graphene grown by chemical vapor deposition (CVD) and integrated with split bow-tie antennae. These direct detectors are capable of room-temperature rectification of a 0.6 THz signal and achieve maximum optical responsivities of 13.0 V/W and 9.1 V/W and minimum noise-equivalent power (NEP) of 530 pW/Hz$^{0.5}$ and 490 pW/Hz$^{0.5}$ for the CVD and exfoliated detectors, respectively. These results are a significant improvement over previous work done with graphene direct detectors and are comparable to other established direct detector technologies. This is the first time room temperature direct detection has been demonstrated using CVD graphene, and because large-area graphene can be produced by CVD growth, scalable graphene detector production is now a possibility.

Acknowledgements

I would first like to thank my supervisor, Professor Jan Stake, for giving me the opportunity to work on this thesis. With his support this has been a fruitful and rewarding project. I would also like to thank Michael Andersson, without whom this project would have been impossible. His daily guidance and patience throughout the past months have been invaluable. As someone who had very little previous knowledge of microwave engineering, I am extremely grateful for Michael's explanations and mini-lessons to bring me up to speed. He always provided constructive feedback as well as positive support, and I consider myself lucky to have had the chance to work with him.

I would thirdly like to thank Maris Bauer, Alvydas Lisauskas, and Professor Hartmut Roskos at the Physikalisches Institut of the Johann Wolfgang Goethe Universität in Frankfurt am Main, Germany for their collaboration on this project. Thanks to Maris for the antenna design and discussion throughout the work, thanks to Alvydas for his help with the measurements, and thanks to the Roskos group for hosting Michael and I during our trip to Frankfurt.

I thank my co-promoter at KU Leuven, Professor Marc Heyns, for his willingness to evaluate this thesis. Thanks also to Professor Guido Groeseneken, Professor Göran Johansson, and Ms. Elke Delfosse for their coordination of the EMM Nano program. I would also like to thank my friends that I have studied with during these past two years in the EMM Nano program for their help and support. I know we will be friends for many years to come.

Finally, I wish to thank my mom, dad, and sister for their unconditional love and support throughout this master's program and this thesis. I am forever grateful.

Audrey Zak

Gothenburg
June 2014

Contents

Abstract **i**

Acknowledgements **iii**

1 Introduction **1**
1.1 Thesis outline . . . 2

2 Theoretical Background **3**
2.1 Electronic properties of graphene . . . 3
2.1.1 Band structure . . . 3
2.1.2 Carrier transport in graphene . . . 4
2.2 Graphene FETs . . . 5
2.3 Terahertz direct detectors . . . 6
2.3.1 Resistive self-mixing . . . 6
2.3.2 Plasma wave generation . . . 8
2.4 Prospects of graphene . . . 9

3 Fabrication and measurement **10**
3.1 Graphene preparation . . . 10
3.1.1 Mechanical exfoliation . . . 10
3.1.2 Chemical vapor deposition and transfer . . . 11
3.1.3 Verification of single-layer graphene . . . 12
3.2 Antenna and GFET design . . . 13
3.3 Process flow . . . 16
3.4 Measurement setup . . . 18

4 Results and Discussion **19**
4.1 DC Characterization . . . 19
4.1.1 Model and extracted parameters . . . 19
4.1.2 Reliability of GFETs . . . 23
4.2 High-frequency measurements . . . 24
4.2.1 Optical responsivity . . . 24
4.2.2 Noise-equivalent power . . . 28
4.2.3 Beam profile . . . 32

5 Conclusions **34**
5.1 Future work 34

Bibliography **36**

1

Introduction

THE RECENT EXPLOSION of research related to the novel two-dimensional material graphene suggests that the possibilities for graphene-based applications are enormous [1, 2]. More specifically, there has been great interest in exploiting the unique electronic properties of graphene for next-generation electron devices. Graphene's remarkable intrinsic properties have attracted researchers from a diverse range of fields, the high-frequency electronics community included.

A multitude of applications rely on the use of the high-frequency portion of the electromagnetic spectrum, specifically the microwave (300 MHz – 30 GHz), submillimetre (30 GHz – 300 GHz) and, increasingly, the terahertz (THz) (loosely defined as 0.3 THz – 3 THz) frequency regions of the spectrum [3]. However, until recently, a lack of technologies capable of operating at THz frequencies led to this region between the optical and microwave regions being referred to as the *terahertz gap* due to the few, niche applications using THz radiation. As the use of the microwave region increases, the push to develop technology to fully utilize the THz region also increases. While traditional applications in the THz were limited to specialized materials operating under extreme conditions, lately the development of devices operating at room temperature has increased. Already, THz applications are found in radio astronomy [3], security imaging [4], explosives detection [5, 6], medical imaging [7, 8], and even anthropology [9].

A challenge thus far in the widespread implementation of THz technology has been a lack of both sources (emitting THz radiation) and detectors (receiving THz radiation) operating at room temperature [10]. In the realm of room-temperature THz detectors, semiconductor materials have dominated the field [11, 12, 13] due to their ready integration with CMOS processing technologies. However, given the recent interest in graphene and its compatibility with CMOS processing, THz detectors based on graphene are emerging [14, 15, 16]. *Direct detection* is the read-out of a voltage or current response from a detector with THz radiation incident on it. Direct detection is desirable from an application perspective because of the straightforward operation of a direct detector. A large amount of research focuses on direct detection at room temperature and a wide variety of materials

and frequencies are studied, making it difficult at times to compare various technologies. Often, the figure-of-merit used to evaluate the sensitivity of a detector is the noise-equivalent power (NEP). The NEP is the ratio of the detector noise to the incident power (THz radiation) it receives and represents the lower limit of the power of the signal that the detector is capable of rectifying without being dominated by the detector's voltage noise. The lower the NEP, the more sensitive the detector. Some representative results of the state-of-the-art are reported in Table 1.1. For graphene, the goal is to demonstrate that it could be competitive with the existing technologies at THz frequencies as has been hoped.

Table 1.1: Comparison of values reported in literature for room-temperature THz detectors.

Technology	Frequency (THz)	NEP (pW/Hz$^{0.5}$)	Source
250-nm Si CMOS array	0.65	300	[12]
150-nm Si CMOS	0.58	42	[13]
InGaAs Schottky diode	0.1–2	20–30	[17, 18]
YBCO bolometer	0.4	200	[19]
Bilayer graphene FET	0.38	$\sim$2000	[16]

Until this thesis, room-temperature direct detection in graphene had not been studied at frequencies above 0.38 THz or using CVD graphene. Room-temperature rectification of a 0.6 THz signal using detectors based on CVD and exfoliated graphene has been successfully demonstrated and record-low NEP has been achieved for graphene detectors, bettering the graphene detector NEPs in 1.1 by an order of magnitude. The scalability of the CVD graphene process implies that the production of sensitive, graphene-based detectors could also be scaled, a viable option for expanding the use of THz technology.

1.1 Thesis outline

Chapter 2 describes the properties of graphene and its potential for use in high-frequency applications. *Chapter 3* explains the device design and fabrication and measurement setup. *Chapter 4* presents the results of DC and terahertz measurements and discusses the implications of those results. Finally, *Chapter 5* recapitulates the important conclusions of this work as well as the prospect for future research.

2

Theoretical Background

GRAPHENE WAS DESCRIBED theoretically in 1947 [20] but thought to be thermodynamically unstable until it was successfully produced by micromechanical cleavage from bulk graphite in 2004 [1]. Graphene is a single, two-dimensional (2D) layer of its parent material, graphite, and graphene sheets are held together by weak van der Waals forces to form the three-dimensional (3D) graphite structure. The weak interactions between layers of graphene make it possible to separate graphite into single graphene sheets. Single-layer graphene (subsequently referred to as simply *graphene*) has unique properties that are a result of its 2D structure. The transport properties of graphene, predicted long ago and more recently experiementally verified, make it a promising material for electronic applications.

2.1 Electronic properties of graphene

2.1.1 Band structure

Graphene is a two-dimensional, honeycomb lattice of sp^2-hybridized carbon atoms as depicted in Figure 2.1. To derive the electronic band structure of graphene using a quantum mechanical approach, a tight-binding Hamiltonian is used. This approach accounts only for nearest-neighbor electron hopping and results in an energy dispersion relation described by Equation 2.1,

$$E_{\pm}(\mathbf{k}) = \pm t\sqrt{3 + 2\cos\left(\sqrt{3}k_y a\right) + 4\cos\left(\frac{\sqrt{3}}{2}k_y a\right)\cos\left(\frac{3}{2}k_x a\right)}, \qquad (2.1)$$

where t is the hopping energy and a is the lattice constant. In graphene, the lattice constant is simply the carbon-carbon interatomic distance between nearest neighbors, so $a \approx 1.42\,\text{Å}$. The positive solution corresponds to the energy dispersion (band structure) of the conduction band, while the negative solution corresponds to the valence band. A diagram of the graphene band structure is shown in Figure

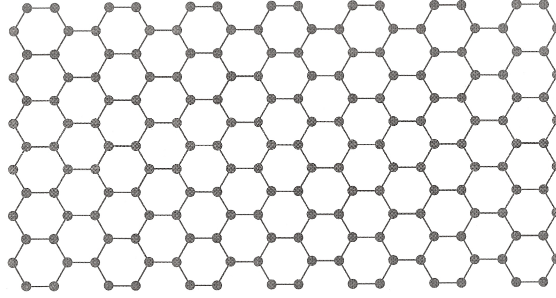

Figure 2.1: Representation of the graphene lattice structure.

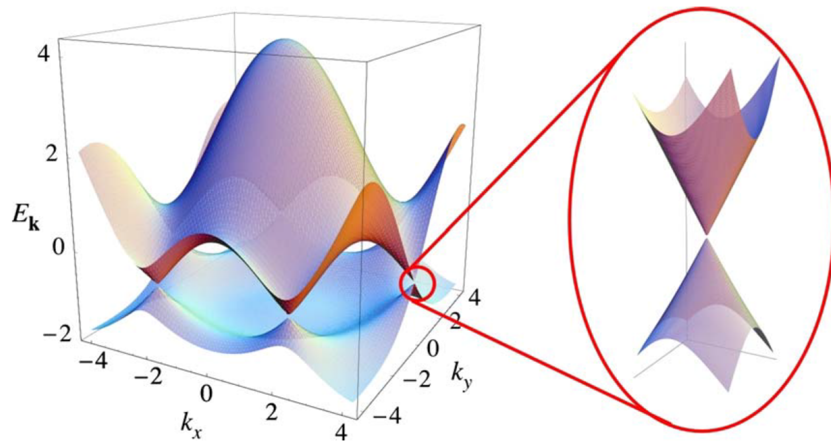

Figure 2.2: The electronic energy dispersion of graphene calculated using a nearest-neighbor hopping energy of $t = 2.7\,\text{eV}$. The zoom shows the energy dispersion near a Dirac point.

2.2 (from [21]). At the edges of the Brillouin zone, represented by the points K and K' in k-space, the conduction and valence bands meet at a single point. These points are called the Dirac points and near them the energy dispersion is linear, such that Equation 2.1 simplifies to

$$E_{\pm}(\mathbf{K}) = \pm v_F |\mathbf{K}|, \tag{2.2}$$

where $\mathbf{K}$ is the momentum relative to the Dirac points and v_F is the Fermi velocity, given by $v_F = 3ta/2 \approx 1 \times 10^6\,\text{m/s}$. This linear energy dispersion has important implications for the electronic properties of graphene. The effective mass of electrons is defined as the second derivative of $E(\mathbf{k})$ near the band edges. Because $E(\mathbf{k})$ is linear where the conduction and valence band meet, this results in an effective electron mass of zero, which means that electrons in graphene behave as massless particles, called massless Dirac fermions.

2.1.2 Carrier transport in graphene

The massless Dirac fermions in graphene should behave, then, as relativistic particles. A consequence of this is a high carrier mobility (for both electrons and holes)

and high carrier saturation velocity. The saturation velocity is the maximum speed at which a charge carrier (a hole or electron) can move through a material when a high electric field is applied. Mobility is related to the saturation velocity in that it is the proportionality constant relating the velocity of the carrier to the electric field by $v_d = \mu E$, where v_d is the drift velocity of the charge carrier. In the case of graphene, near the intersection of the conduction and valence bands, the charge carriers move at the Fermi velocity v_F, which leads to a high mobility μ even at low applied fields. It has been shown experimentally that the charge carriers can propagate micrometer distances without scattering [1] which should lead to ballistic transport in very short devices.

While the calculated values of mobility are high, many factors can act to degrade the mobility, including impurities, lattice defects, and substrate interactions [22]. The mobility of graphene on SiO_2 has been shown to be temperature-independent and as high as $10{,}000\,\mathrm{cm^2/V\,s}$ [1], but in practice this is difficult to achieve. Residues left on graphene as a result of processing act as scattering centers for carriers, reducing mobility [23]. Surface phonons from the substrate also scatter carriers, even at low temperatures and on various substrate materials [24]. On substrates with better lattice-matching to graphene, like hexagonal boron nitride, graphene mobility can be as high as $25{,}000\,\mathrm{cm^2/V\,s}$ [25]. Suspended graphene has also been studied in an effort to eliminate substrate effects altogether [26]. The advantage of SiO_2 as a substrate is that graphene is visible on SiO_2 in an optical microscope while it is transparent on other substrates [27].

2.2 Graphene FETs

The energy band structure of graphene makes it an interesting channel material in an FET. In unbiased graphene, the Fermi level lies at the Dirac point, with the conduction band completely filled and the valence band empty. This makes graphene a zero-gap material and results in an electric field effect with both electrons and holes as charge carriers [2]. By applying a bias to the graphene via a gate, the Fermi level can be lowered into the conduction band (negative gate voltage) or raised into the valence band (positive gate voltage). A Fermi level in the valence band results in holes as the charge carriers; conversely, a Fermi level in the conduction band results in electrons as the majority carriers. Figure 2.3 shows the resistivity of a graphene FET and the position of the Fermi level on either side of the Dirac point. The demonstration of the electric field effect in graphene and graphene's compatibility with CMOS processing techniques allows the straightforward fabrication and operation of graphene FETs (GFETs).

The carrier mobility and high carrier saturation velocity in graphene translate to a high cut-off frequency f_T at radio frequencies. This has allowed GFETs to be successfully implemented in high-frequency electronics [28, 29, 30, 31]. However, while GFETs have been demonstrated at microwave frequencies, the carrier transit time limits the cut-off frequency that can be achieved, since f_T scales roughly as the inverse of transit time. In order to use GFETs as detectors at THz frequencies, the transit-time limit must be overcome.

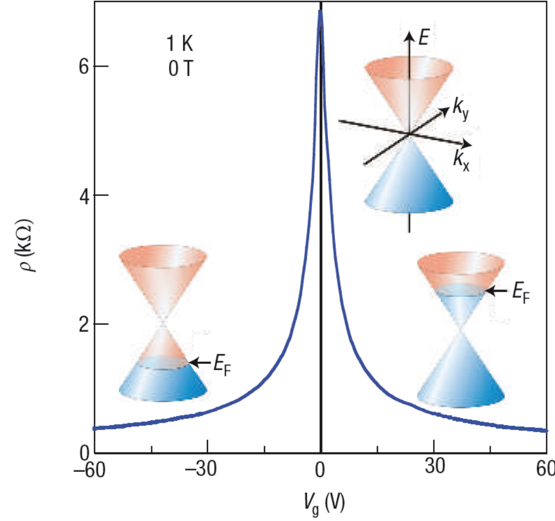

Figure 2.3: Resistivity of graphene at a temperature of 1 K and zero applied magnetic field. Representations of energy bands show how the position of the Fermi level changes as a function of gate voltage (from [2]).

2.3 Terahertz direct detectors

2.3.1 Resistive self-mixing

Detection of high-frequency radiation by a FET is based on frequency mixing in the FET channel [32]. Mixing a radio-frequency (RF) input signal with a local oscillator (LO) signal at the ports of the transistor generates a drain current. The time-dependent input voltage (of the RF signal) is taken to be

$$v_{\mathrm{RF}}(t) = V_{\mathrm{RF}} \sin(\omega t) \tag{2.3}$$

where ω is the frequency of the RF signal. By taking advantage of the nonlinear properties of a transistor, specifically the transconductance g_m, the FET can act as a mixer. When the DC gate bias V_G is near the point where the transconductance is zero, the nonlinearity of the transconductance means that a small change in gate voltage causes a large change in transconductance. Applying a LO signal to the gate when the gate bias is such that the transconductance is almost zero allows the FET to be switched between high and low transconductance states, with switching occurring at the LO frequency. Knowing the transconductance and the signal voltage, the channel current can be calculated as the product of the two as

$$i_{DS} = v_{\mathrm{RF}}(t) g_m(t). \tag{2.4}$$

The transconductance is time-dependent because it switches at the LO frequency. In general, the transconductance can be expressed as a Fourier series of the harmonics (integer multiples) of the LO signal as in Equation 2.5.

$$g(t) = g_0 + 2\sum_{n=1}^{\infty} g_n \cos n\omega_{\mathrm{LO}} t \tag{2.5}$$

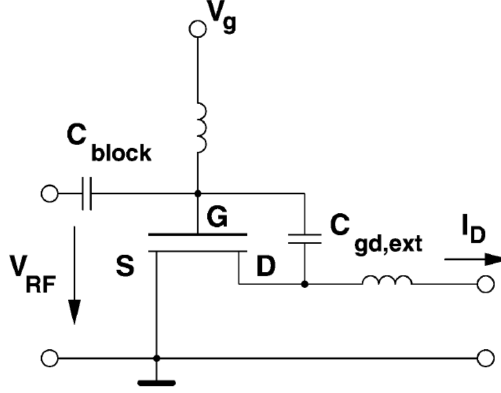

Figure 2.4: FET circuit used in conceptualization of resistive mixing (from [12]). The inductor at the gate acts as an RF choke so that DC gate bias may be applied, and the corresponding capacitor C_{block} blocks shorts the RF signal and blocks the DC signal, resulting in both a DC and RF voltage at the gate.

For a FET, the first Fourier coefficient ($n = 1$), g_m, can be written in terms of the RF voltage and the transistor characteristics of channel width W, channel length L, mobility μ, oxide capacitance per unit area C_{ox}, and threshold voltage V_{th} as

$$g_m(t) = \frac{W}{L}\mu C_{ox}[v_{\text{RF}}(t)/2 + V_G - V_{th}]. \tag{2.6}$$

Then, combining Equations 2.4 and 2.6 the current depends on the square of the input voltage as in Equation 2.7.

$$i_{DS} = \frac{W}{L}\mu C_{ox}[v_{\text{RF}}(t)^2/2 + v_{\text{RF}}(t)(V_G - V_{th})] \tag{2.7}$$

Direct detection of terahertz radiation has been demonstrated in silicon FETs and explained by the principle of resistive self-mixing in the FET channel [12]. The description is based on the circuit shown in Figure 2.4, where the source is grounded and the gate and drain are connected by a gate capacitance $C_{gd,ext}$. In terms of high-frequency electronics, the drain is the RF port and the gate is the LO port. The gate capacitance couples the THz signal to the gate and drain simultaneously (hence the term *self*-mixing), and it is the coupling of the RF and LO ports that allows for the mixing to take place. This configuration results in homodyne detection, meaning that the LO signal is at the same frequency as the RF signal. By the assignment of gate and drain as LO and RF ports, it is possible to say then that

$$v_{DS} = v_{\text{RF}} \tag{2.8}$$

and

$$v_{GS} = v_{\text{RF}} + V_G. \tag{2.9}$$

A DC drain-source current I_{DS} is generated, given by Equation 2.10, where

$$I_{DS} = \frac{W}{L}\mu C_{ox}\frac{V_{\text{RF}}^2}{4} \tag{2.10}$$

and the input voltage v_{RF} is given by Equation 2.3. Dividing I_{DS} by the DC channel conductance G_m (where the v_{RF}-dependence in g_m drops out) gives the drain-source voltage V_{DS} generated as a function of the input voltage

$$V_{DS} = \frac{I_{DS}}{G_m} = \frac{\frac{W}{L}\mu C_{ox}\frac{V_{\mathrm{RF}}^2}{4}}{\frac{W}{L}\mu C_{ox}(V_G - V_{th})} = \frac{V_{\mathrm{RF}}^2}{4(V_G - V_{th})}. \tag{2.11}$$

The current response given by Equation 2.7 and the voltage response given by Equation 2.11 are a result of the incident radiation, which is the basis for detection of high-frequency signals in a FET. Dividing the response by the power that the detector receives gives the *responsivity*. The responsivity is a good metric for comparing the performance of different detectors because system-specific incident power does not have an influence.

2.3.2 Plasma wave generation

The theory of detection of THz radiation by plasma waves (instead of resistive mixing) in a FET was put forth by Dyakonov and Shur in 1996 [33] based on the behavior of the two-dimensional electron fluid in a FET. Their explanation is based on earlier theoretical work describing the mechanism for plasma wave generation in a ballistic FET [34] in that the electrons act not as individual particles but instead as an electron *fluid* in a ballistic FET. Here, the designation that the FET is *ballistic* is important because it implies that the electrons do not experience collisions in the FET channel. This electron fluid can be analogously described by the hydrodynamic equations for shallow water, where the waves in the analogy refer to the plasma waves of the electron fluid.

FETs in which plasma waves are generated in the channel can operate at higher frequencies than conventional devices because the plasma waves in the channel propagate much faster than electrons. This means that these devices are not limited by electron transit time. Detection of THz radiation in these devices is possible through the constant drain-source voltage that is generated by the incident THz radiation. The THz radiation causes plasma wave excitation at the source, which induces an ac current, which is then rectified and measured as a dc signal at the drain. It follows that there must be some asymmetry introduced in the coupling of the source and drain to the channel for plasma waves to be preferentially generated at only one of the channel boundaries (in the absence of an applied source-drain bias). Because the THz radiation modulates both the carrier drift velocity and the carrier concentration in the channel, the drain-source voltage detected can be further tuned at a given incident frequency by adjusting the carrier concentration by gating the channel [35].

As with any wave confined between fixed boundary conditions, at certain frequencies a standing wave will form. In the context of THz detection, this is referred to as *resonant detection* because at the resonant frequency (and its odd harmonics) the drain-source voltage will reach its maxima. To establish criteria for resonant detection, both the frequency of the plasma waves in the channel as well as their propagation must be examined. The frequency of the plasma waves is taken as the frequency of the incident radiation, called ω. The factor governing the

plasma wave propagation in the channel is the scattering relaxation time τ, which represents the average time between carrier collisions with phonons or impurities. The scattering time depends on the mobility μ as

$$\tau = \frac{\mu m}{e} \tag{2.12}$$

where m is the electron mass and e is the elementary charge. This theory assumes that the mobility is constant, but in reality the mobility is dependent on the gate voltage [36]. However, for the sake of simplicity the mobility will be assumed to be a constant, material parameter. The behavior of the plasma waves in the FET channel falls into different regimes, determined by the quantity $\omega\tau$. If $\omega\tau \gg 1$, then the plasma waves will experience only weak damping, and resonant detection will occur if the channel is short. The condition for channel length is defined by $s\tau/L$, where s is the plasma wave velocity and is determined by the applied gate bias, and L is the channel length. If both $\omega\tau \gg 1$ and $s\tau/L \gg 1$, then resonant detection will occur at the fundamental plasma frequency ω_0 and its odd harmonics n, given by

$$\omega_0 = \frac{n\pi s}{2L}. \tag{2.13}$$

If the length condition is not satisfied, meaning that $L \gg \omega\tau$, the plasma waves will decay before they reach the end of the channel, and no standing wave will form. These plasma waves are underdamped and the detection will be broadband. For the case where $\omega\tau \ll 1$, the plasma waves are overdamped and will decay at the source. The detection will also be broadband. Therefore, in order for resonant detection to be possible, either the channel mobility must be high or the frequency of the signal must be high. Due to the limited availability of high-frequency sources operating above 1 THz, the search for room-temperature resonant detection has focused on maximizing the mobility of the channel material. Graphene's room-temperature mobility has made it a candidate for resonant detection, but as of yet a conclusive demonstration of resonant detection at room temperature has not been observed in any material, although work with GaAs has come close [37].

2.4 Prospects of graphene

Graphene's unique electronic structure has made a variety of novel electronic devices possible, but there are still significant obstacles to overcome. In theory, the mobility of carriers and the carrier velocity in graphene are extremely high, but when implemented in a device these properties are rarely seen at room temperature. Already, respectable results have been obtained for graphene detectors, and as graphene processing techniques and mobility manipulation continue to improve graphene has the potential to be competitive with other state-of-the-art high-frequency materials.

3

Fabrication and measurement

3.1 Graphene preparation

A number of methods to produce single-layer graphene have been developed [1, 38, 39] and two have been used in this thesis work. The most straightforward method is mechanical separation of graphene flakes from multilayer graphite. The second method used was graphene growth by chemical vapor deposition (CVD) on a copper foil catalyst.

3.1.1 Mechanical exfoliation

Because the forces between layers of graphene are weak, individual layers can be separated from graphite and transferred to a desired substrate using minimal force and standard laboratory tape. This micromechanical cleavage of graphene layers is referred to as the *mechanical exfoliation* of graphene. Although graphene is nearly optically transparent (absorbing only 2.5 % in the visible range), when single layer graphene is placed on top of silicon dioxide of the appropriate thickness, interference with white light causes sufficient contrast to identify single-layer graphene in an optical microscope. In white light, oxide thicknesses of either 90 or 300 nm allow identification of single layer graphene on SiO_2 [27]. In this work, high-resistive silicon wafers with an oxide thickness of 300 nm were used for all samples.

Figure 3.1 shows an optical microscope image of a typical graphene flake produced by mechanical exfoliation. The lightest blue area on the right side of the flake is a single layer, while the darker blue areas are a few or even tens of layers. While there is contrast between the single-layer graphene and the SiO_2, it is faint and makes identification of single-layer graphene difficult. Before exfoliation, 10 mm × 10 mm Si/SiO_2 substrates were cleaned in acetone, methanol, and isopropanol and then an oxygen plasma ash to remove any organic contaminants. Wafer dicing tape was pressed onto bulk graphite and then gently pressed onto the clean substrates. By repeated pressing and sticking, the graphite should separate into thinner and thinner stacks of layers until some single-layer graphene

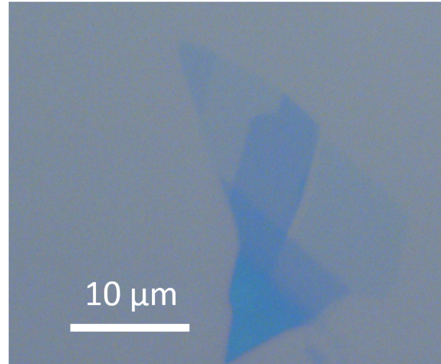

Figure 3.1: Optical microscope image of exfoliated graphene flake showing single- and multi-layer areas.

is deposited on the substrate. Careful examination under white light in an optical microscope allowed identification of single-layer graphene. The position of single-layer flakes on the sample was recorded for later patterning steps. While mechanical exfoliation of graphene allows optical identification of flakes potentially useful for applications, because the position and size of the flakes cannot be controlled it is a low-yield process.

3.1.2 Chemical vapor deposition and transfer

The growth of graphene on copper foil by chemical vapor deposition (CVD) allows the possiblity for large-area, single-layer graphene. Following the recipe in [40], a thin copper foil (50 μm) is used as a catalyst for growth. Prior to graphene growth, the copper foil is cleaned in isopropanol and acetic acid to remove contaminants and native oxide. Graphene growth is carried out in a cold-wall, low-pressure CVD reactor (Black Magic, AIXTRON Nanoinstruments, Ltd.). The clean Cu is heated to 1000 °C inside the reactor and annealed for 5 minutes in a flow of 20 sccm H_2 and 1000 sccm Ar gases. This annealing increases the copper grain sizes, which ultimately improves the graphene quality. After annealing, the precursor gas, high-purity methane diluted to 5 % in argon, is introduced to the chamber at a flow rate of 30 sccm for 5 minutes. Because the solubility of carbon in copper is low, the CVD reaction is nearly self-limiting to a single graphene monolayer.

After growth on the Cu catalyst, the graphene is transferred to an Si/SiO_2 substrate via the H_2 bubbling transfer method depicted in Figure 3.2 (from [41]). First, a PMMA polymer photoresist film is spin-coated onto the graphene on copper foil. A plastic frame is glued to the PMMA surface using additional PMMA photoresist. The entire stack is submerged in an electrochemical cell with a platinum anode and NaOH/H_2O electrolyte solution. A 1 V potential is applied between the platinum anode and copper cathode, driving the hydrolysis of water. The water hydrolysis causes H_2 gas bubbles to form at the surface of the Cu foil, and the bubbles gently separate the graphene/PMMA/frame stack from the Cu foil. After the graphene/PMMA/frame is separated from the Cu, it is rinsed in deionized water and placed on a clean Si/SiO_2 substrate. Once dry, the frame is cut away using a scalpel and the remaining PMMA on top of the graphene is

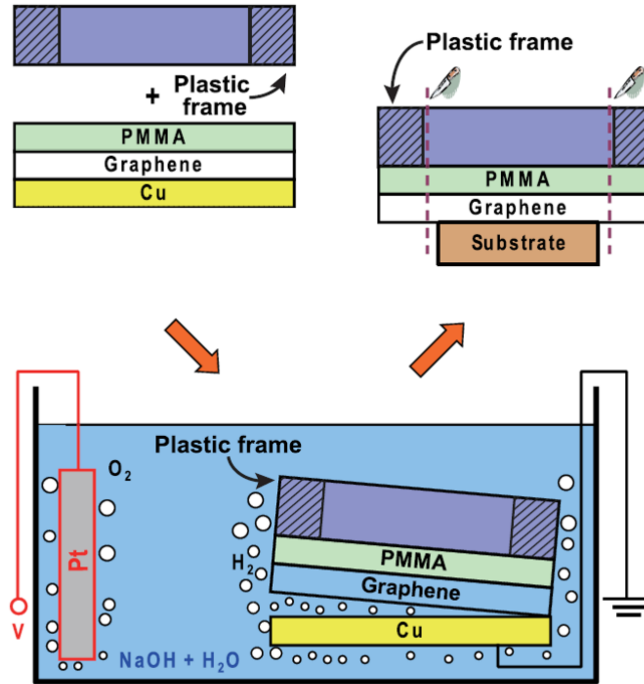

Figure 3.2: Schematic of the hydrogen-bubbling method used to separate CVD graphene from the Cu catalyst and transfer it to the desired substrate.

dissolved in acetone. In this work, the Si/SiO_2 substrates were 10 mm × 10 mm and graphene films were successfully transferred without significant tears or wrinkles, indicating that this frame-assisted transfer process is suitable for large-area samples.

3.1.3 Verification of single-layer graphene

While examination with an optical microscope is a fast way to find single-layer graphene, because of the low resolution of the microscope and the low contrast between the graphene and the SiO_2, it can be difficult to distinguish single-layer graphene from bilayer or few-layer graphene. To confirm that the graphene is indeed a single layer, Raman spectroscopy was performed. Figure 3.3 shows the Raman spectra of the exfoliated and CVD graphene. The D peak in the spectra corresponds to the disorder in the graphene lattice, and the absence of the D peak in the exfoliated sample indicates that the graphene is structurally highly ordered. The G peak is the result of the interaction of the incoming light (in the Raman setup) with the sp^2-hybridized carbon atoms of the graphene. It is the 2D peak that indicates that the graphene is a single layer [42] as it is a narrow peak, not showing any splitting. The more graphene layers present, the wider the 2D peak becomes because the incident Raman photons interact with a greater number of energy bands as more layers are added. The narrow 2D peaks in the spectra of Figure 3.3 (full-width at half maximum of 30 cm^{-1} and 34 cm^{-1} for the exfoliated and CVD graphene, respectively) show that the graphene used in the GFET fabrication is in fact a single layer.

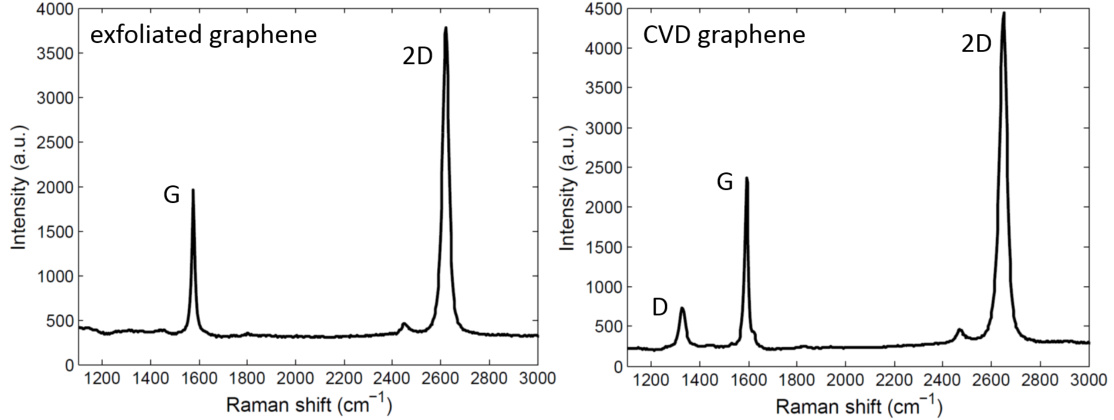

Figure 3.3: Raman spectra of the exfoliated and CVD graphene with the key peaks labeled, with the D peak at 1350 cm^{-1}, the G peak at 1590 cm^{-1}, and the 2D peak at 2650 cm^{-1}.

3.2 Antenna and GFET design

Split bow-tie antennae were designed by Maris Bauer (Physikalisches Institut, Johann Wolfgang Goethe-Universität) to couple radiation at a frequency of 0.6 THz. The designs were based on previous work done by the Roskos group at Johann Wolfgang Goethe Universität [43] using bow-tie antennae, but never before had these antennae been integrated with a GFET for direct detection. The antenna bows act as the GFET electrodes, simultaneously applying gate bias as well as allowing read-out of the rectified signal at the drain. Figure 3.4 shows a drawing of the antenna design, including the contact pads used for electrical probing. In their previous work, Bauer *et al.* had success with the bow-tie antenna when they used a double-gate transistor design. However, for the present work, it was decided that a single transistor would be used. In order to have THz rectification by plasma waves, there must be asymmetric coupling to the transistor feeds (source and drain). This means that a single transistor with a conventional bow-tie antenna would not rectify THz signal because the coupling to each of the antenna bows is symmetric. To create the asymmetry required for rectification, the split bow-tie design (one antenna bow is split into gate and drain) was implemented.

An advantage of the bow-tie antenna is its broadband characteristic. This means that the detectors should have a response over a relatively wide range of frequencies, instead of resonant detection around a single frequency. The overall dimension of the antenna was designed for measurement at a frequency of 0.6 THz. Roughly, the diameter of a bow-tie antenna should be half the wavelength of the incident radiation for good detection. Additionally, impedance matching with the graphene channel was considered, based on the impedance of CVD GFETs previously studied [30] and an antenna impedance of 100 Ω. Two different designs were studied, referred to from here on as the *simple* and *finger* designs. The simple design, shown in the lower left corner of Figure 3.4 was fabricated in two variations: the first had a gate width W_g of 2 μm and the second had a gate width of 5 μm. Both had a gate length L_g of 2.5 μm.

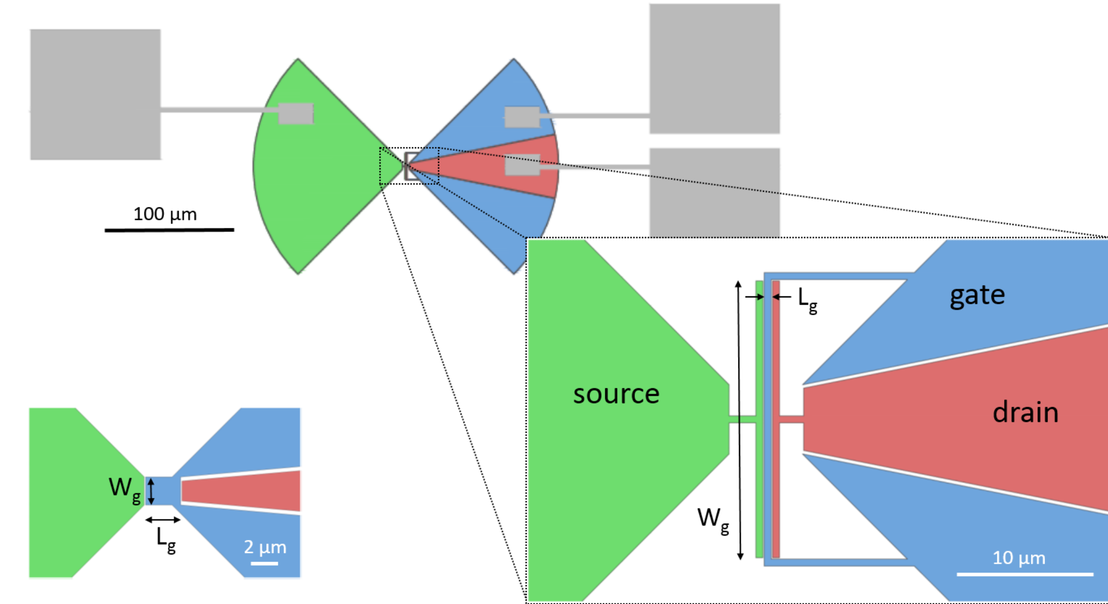

Figure 3.4: Bow-tie antenna designs for the simple (lower left) and finger (lower right) layouts. In both layouts, the source is colored green, the gate is in blue, and the drain is in red. Probing pads for measurement are grey. Relevant device dimensions are indicated, with L_g as the gate length and W_g as the gate width.

The second design, the finger design, is shown in the lower right corner of Figure 3.4 and has a wider gate width and shorter gate length than the simple design. Three variations on this design were fabricated, all with the same gate width of 20 μm. The gate lengths studied were 250 nm, 500 nm, and 1 μm. In order to prevent a large capatitance that would arise from increasing the metal area, the narrow source and drain fingers were designed so that the gate width could be increased without a large increase in parasitic effects. Simulations showed that the simple design had good antenna characteristics but a large impedance mismatch to the device, so the finger design was made in an attempt to more closely match the device impedance while maintaining good antenna characteristics.

Before fabrication, the antenna designs were studied using ADS simulation software. From these simulations, the reflection coefficient S_{11} was estimated and is plotted in Figure 3.5 for both the simple and finger designs. The simulations assumed a device impedance of 50 Ω. Knowing that the available measurement source was at a frequency of 0.6 THz, it was important that S_{11} was minimized near that frequency (indicating that a minimum of incident radiation would be reflected). The wide minima indicate broadband antenna characteristics, which are typical of bow-tie antennas. The finger design with a gate length of 250 nm was predicted to give the best results based on these simulations.

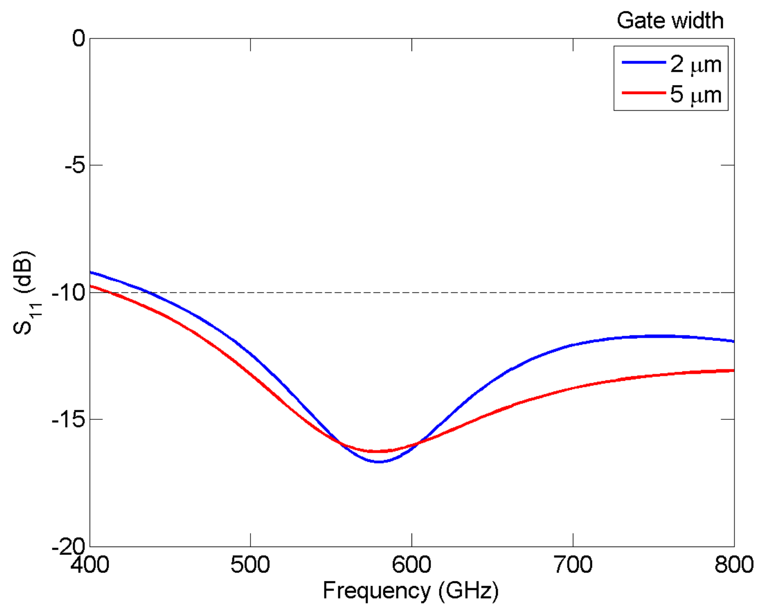

(a) Simple design

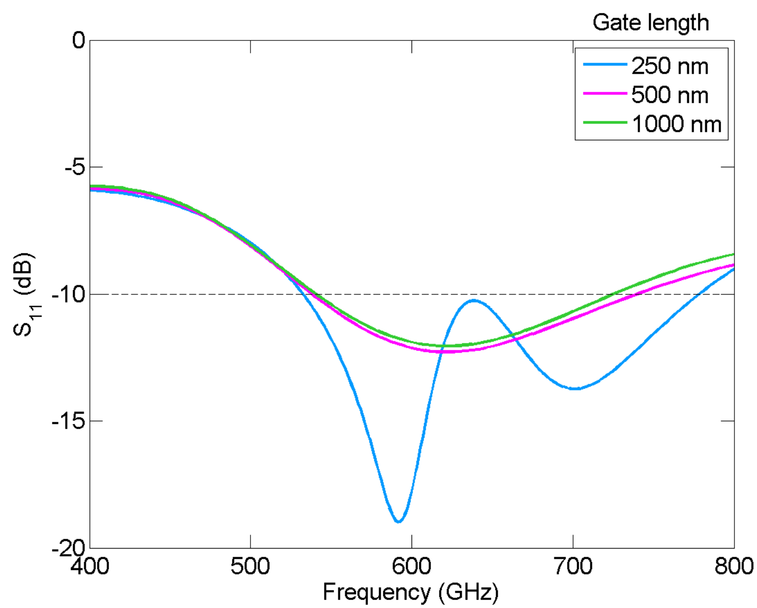

(b) Finger design

Figure 3.5: S_{11} reflection coefficients from simulations performed in ADS.

3.3 Process flow

The antenna designs were patterned on either CVD or exfoliated graphene using electron beam lithography. Figure 3.6 shows the cross-sectional visualization of the process steps performed to fabricate the antennae. Because the size of the antenna bows is large compared to the transistor structure, the diagram is not to scale and is intended only as an illustration of the process steps and layers. The first lithography step is the patterning of the source and drain antenna bows. A bilayer positive resist stack is used (MMA EL 10 and SX/ARP 6200 2:1 in anisole) to give high resolution and ease metal liftoff. After patterning the resist, the source and drain are metallized with 1 nm Ti/15 nm Pd/300 nm Au. The Ti acts as a sticking layer, as Pd and Au make poor contact with graphene. Pd is used to minimize contact resistance, and Au is used as the top layer for it inertness and high conductivity. The gate oxide Al_2O_3 is grown by first evaporating 1 nm Al and then baking on a hotplate at 170 °C for 5 minutes. This is repeated to create a thin (approximately 2 nm) layer of natural oxide, as it adheres well to graphene. A second lithography step is performed to create an etch mask, and then the natural oxide outside the channel is etched in an HCl bath. The graphene outside the channel area is etched in oxygen plasma. Then, 15 nm of Al_2O_3 is grown by atomic layer deposition (ALD) to create the remainder of the gate oxide (Oxford FlexAl Atomic Layer Deposition system) with a final thickness of approximately 17 nm. Following ALD, the gate was deposited with 1 nm Ti/300 nm Au. After the final lithography step, oxide was etched from the source and drain and probing pads were evaporated (1 nm Ti/300 nm Au). The gold thickness of 300 nm was chosen to be much larger than the skin depth of gold at 0.6 THz, which is approximately 100 nm. This ensured that no losses would result in the metal.

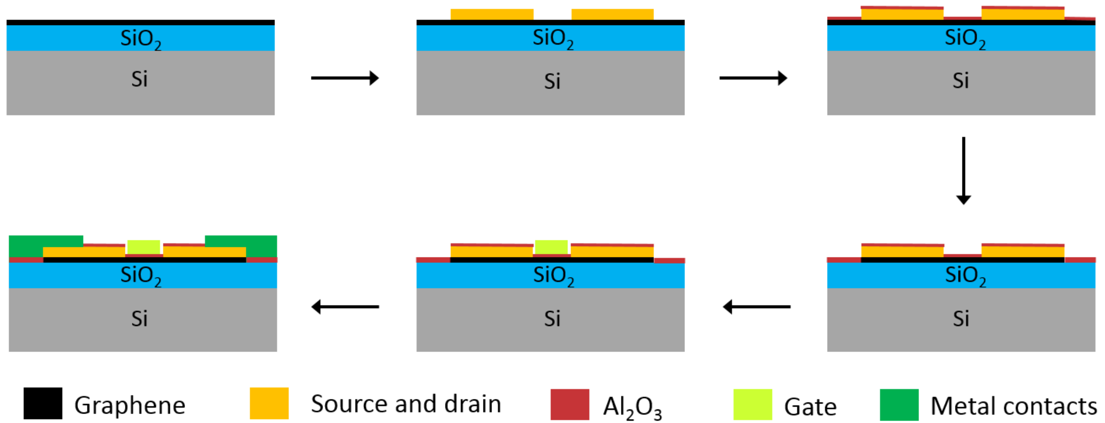

Figure 3.6: Schematic of process steps for the patterning of the bow-tie antennae on graphene.

An SEM image of a device with the simple design (gate width $W_g = 2\,\mu$m and gate length $L_g = 2.5\,\mu$m) with a detail showing the GFET between the antenna bows is shown in Figure 3.7.

Figure 3.8 shows an SEM image of a device with a finger design with a gate length of 250 nm. The area where the graphene was protected from plasma etching

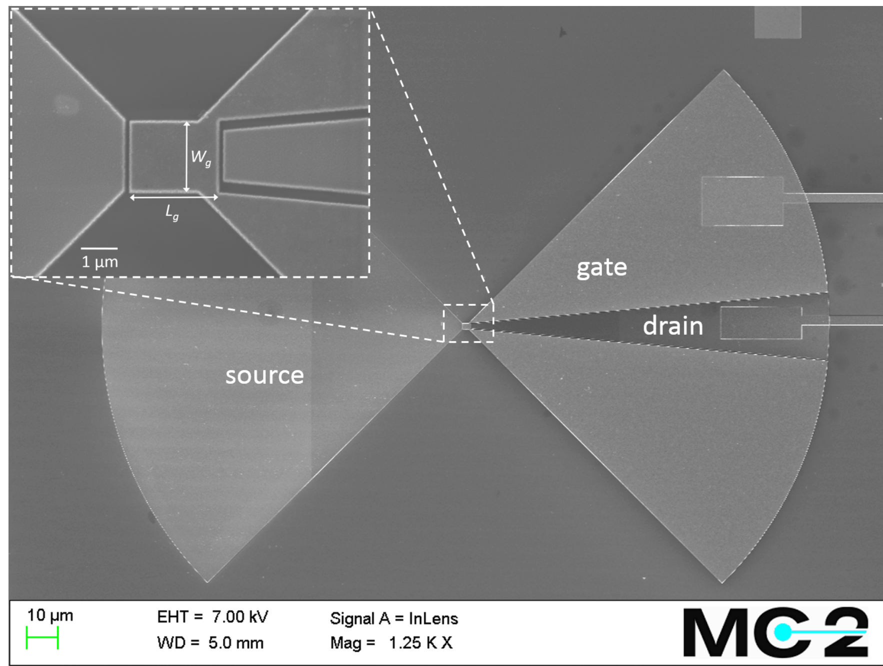

Figure 3.7: Scanning electron microscope (SEM) image of a simple-design device at a magnification of 1250x.

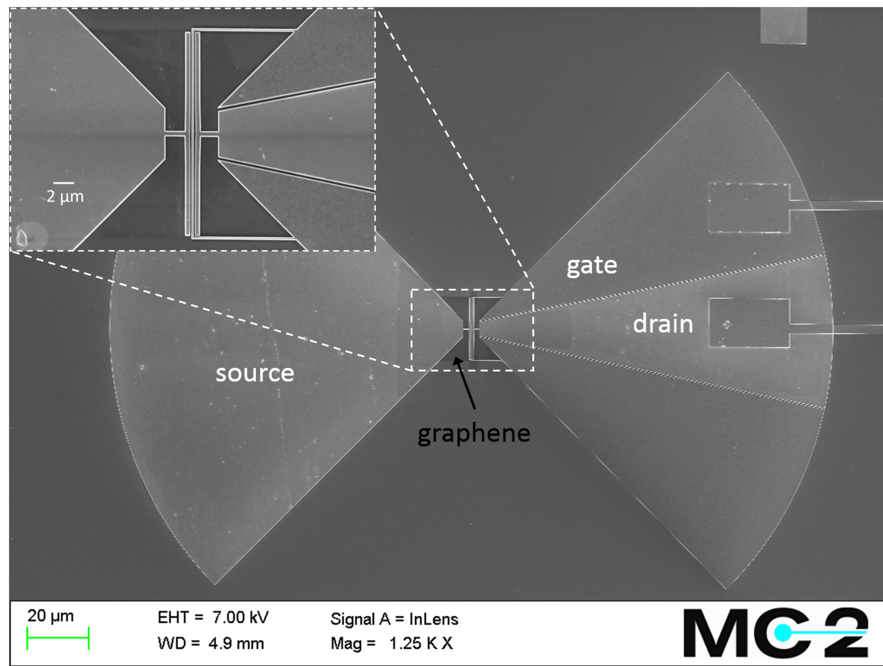

Figure 3.8: Scanning electron microscope (SEM) image of a finger-design device with the graphene visible as a shadow on the substrate at a magnification of 1250x.

is clearly visible as the graphene appears as a dark shadow in the scanning electron microscope. Because graphene is conductive, incident electrons are conducted away through the graphene sheet instead of being trapped and scattering other electrons (which would make the appearance lighter).

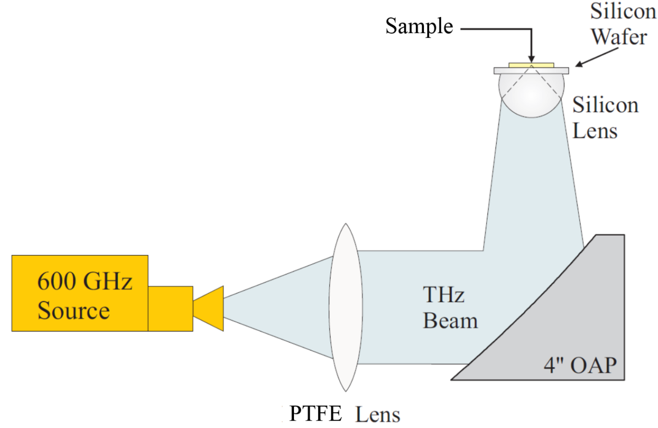

Figure 3.9: Diagram of measurement setup used to characterise the graphene detectors. The silicon wafer on top of which the sample is mounted is on a stage that can be moved by micrometer screws in the x and y directions.

3.4 Measurement setup

DC measurements were made at Chalmers using a Keithley 4200 semiconductor characterization system. Probes were contacted directly to the chip on the contact pads. High frequency measurements were made at the Physikalisches Institut of the Johann Wolfgang Goethe-Universität in Frankfurt, Germany. The sample was placed on a silicon lens and illuminated from below while probes were in contact with the contact pads for read-out. An all-electronic source was driven at 16.385 GHz by an amplitude-modulated synthesizer with a rectangular time signal and a modulation frequency of 333 Hz. This frequency was the reference for lock-in detection. The output of the source is upconverted by a frequency multiplier to an output frequency of 0.6 THz. The output beam was collimated using a Picarin lens and then focused using an off-axis parabolic (OAP) mirror. Further focusing was achieved throught the use of an aplanatic hyper-hemispherical lens underneath the probe station where the sample is mounted. The sample is placed on top of a 440-μm thick silicon wafer on the probe station, which can be moved in the x and y directions to illuminate individual detectors on the sample. A diagram of the measurement setup is shown in Figure 3.9.

The THz beam power was measured using a photo-acoustic Thomas Keating power meter, and the beam power incident on the detector was measured to be 290 μW excluding losses from the silicon lens. When measuring voltage and current responsivity, the beam was attenuated by 10 dB by placing cardboard sheets in its path. This was done to prevent standing waves from forming between the beam source and the detector.

4

Results and Discussion

4.1 DC Characterization

In order to characterize the GFETs before THz measurements were made, DC measurements were performed. Plots of the drain-source resistance R_{DS} (shown in blue) as a function of the gate-source voltage V_G for the simple design are shown in Figure 4.1 and in Figure 4.2 for the finger design.

The overall resistance level is determined by the dimensions of the graphene channel. The resistance is dependent on the resistivity ρ of the graphene (a material property) and the ratio of channel length to width L/W as $R_{DS} = \rho\frac{L}{W}$. This means that for a given gate length, a wider channel will have lower resistance as is seen in the comparison between Figures 4.1(b) and 4.1(c). Both the 5 μm-gate-width GFET and the 2 μm-gate-width GFET have a gate length of 2.5 μm, but the wider GFET has a lower R_{DS}. For a given gate width, a longer channel will have larger resistance, a trend which is illustrated by the resistances shown in Figure 4.2. All devices have a gate width of 20 μm, the shortest device ($L_g = 250$ nm) has the lowest resistance, and the longest device ($L_g = 1000$ nm) has the largest resistance.

The green data points in Figures 4.1 and 4.2 are the calculated transconductance g_m, which is defined as

$$g_m = \left.\frac{\partial I_{DS}}{\partial V_G}\right|_{V_{DS}} \tag{4.1}$$

and describes how the drain-source current I_{DS} varies with the gate voltage V_G at constant drain-source voltage V_{DS}. The better the R_{DS} modulation, the higher the transconductance. For THz detection, it is necessary to have sufficient channel modulation ability to see a significant THz response [44].

4.1.1 Model and extracted parameters

From the R_{DS} data it is possible to extract useful parameters for the GFETs. As previously discussed, for resonant detection to be possible, the mobility of the

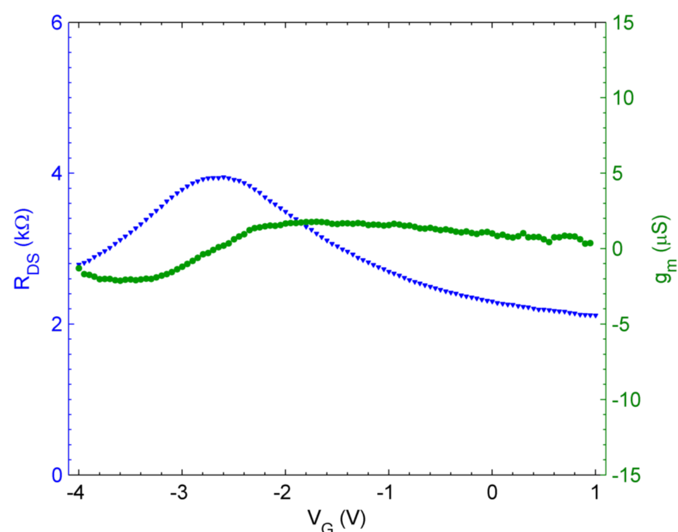

(a) Exfoliated graphene, gate width 2 μm.

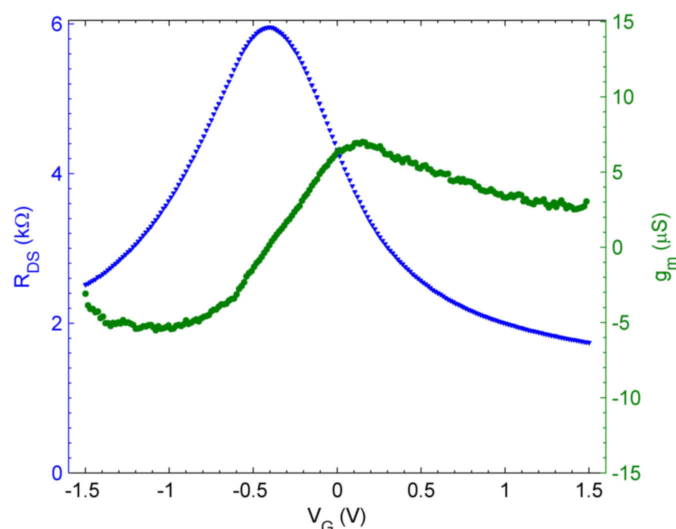

(b) CVD graphene, gate width 2 μm.

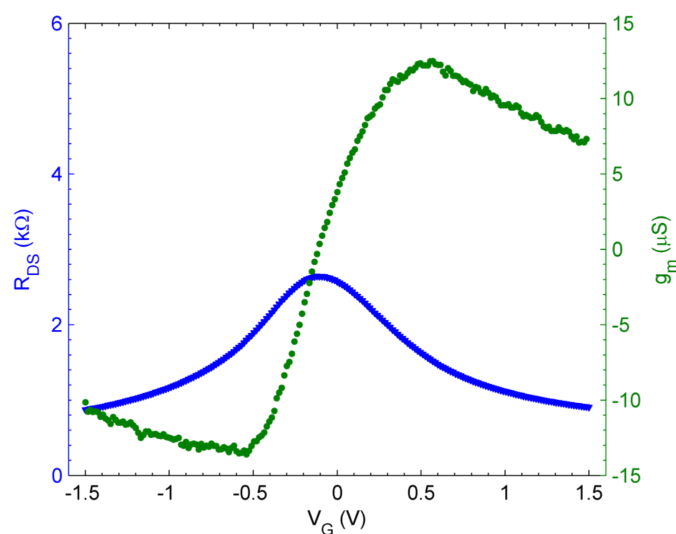

(c) CVD graphene, gate width 5 μm.

Figure 4.1: Drain-source resistance of simple-design GFETs.

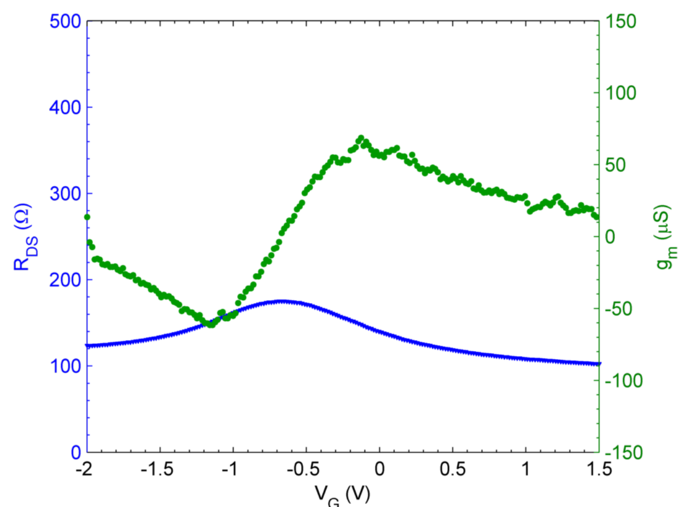

(a) CVD graphene, gate length 250 nm.

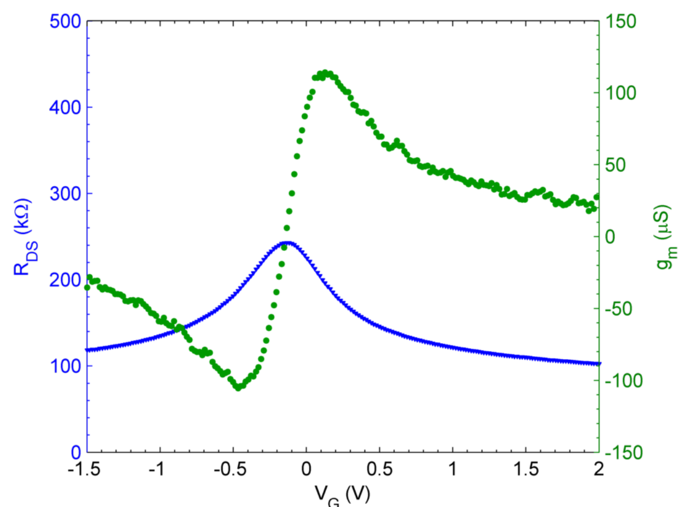

(b) CVD graphene, gate length 500 nm.

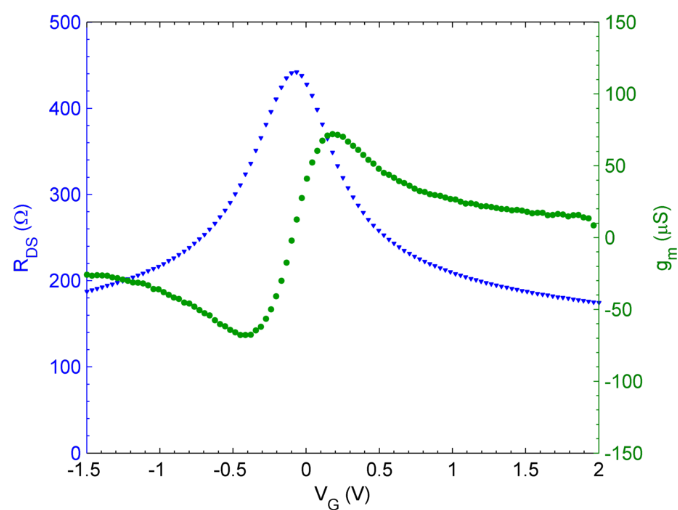

(c) CVD graphene, gate length 1000 nm.

Figure 4.2: Drain-source resistance of finger-design GFETs.

Table 4.1: Summary of dc parameters for the simple-design devices with V_{DS} = 100 mV.

Graphene	W_g (μm)	V_{Dirac} (V)	μ_e, μ_h (cm^2/V s)	max. g_m (μS)
exfoliated	2	−2.60	1900, 1400	1.8
CVD	2	−0.40	2100, 1800	7.0
CVD	5	−0.12	1600, 1900	12.5

FET channel material must be sufficiently high such that the condition $\omega\tau \gg 1$ is fulfilled at a given frequency. For the measurements made here at 0.6 THz, the mobility necessary for resonant detection (not taking into account the influence of the channel length) must be larger than 2900 cm^2/V s for an effective carrier mass of 9.11×10^{-31} kg. Extracting the mobility of the graphene also gives insight into the graphene quality, as defects and impurities degrade the mobility [22].

Following the method in [45], Equation 4.2 is fit to the DC measurement of R_{DS} (in units of Ω) as a function of V_G, where the mobility μ and residual carrier concentration n_0 are fitting parameters. The residual carrier concentration was between 7×10^{11} and 1×10^{12} cm^{-2} for these GFETs, indicating that the graphene was reasonably impurity-free since n_0 of clean graphene on SiO_2 is $\sim 10^{10}$ cm^{-2} [22].

$$R_{DS} = \begin{cases} (R_s + R_d) + \frac{L_g}{W_g q \mu_e \sqrt{n^2+{n_0}^2}} & \text{for electrons} \\ (R_s + R_d) + R_{\text{ext}} + \frac{L_g}{W_g q \mu_h \sqrt{n^2+{n_0}^2}} & \text{for holes} \end{cases} \quad (4.2)$$

R_s and R_d are the source and drain contact resistance and R_{ext} is an extra resistance that arises from the fact that some level of doping in graphene is unavoidable during processing (meaning that $V_{Dirac} \neq 0$) and so the electron and hole branches of the R_{DS} curve are not symmetric. For the devices presented here, $R_s = R_d$ because the source and drain have the same contact area with the graphene channel. The gate length L_g and width W_g as well as the elementary charge q are constant, and the dependence of R_{DS} on the gate voltage V_G comes into the charge concentration n, given by Equation 4.3.

$$n = \frac{C_{\text{gate}}}{q}(V_G - V_{Dirac}) \quad (4.3)$$

The gate capacitance C_{gate} is taken to be 310 nF/cm^2 based on the oxide thickness and dielectric constant of Al_2O_3 [46]. A representative fit to the R_{DS} data is shown in Figure 4.3. The extracted parameters from the fit as well as the Dirac voltage and maximum transconductance are summarized in Tables 4.1 and 4.2 for the simple and finger detectors, respectively.

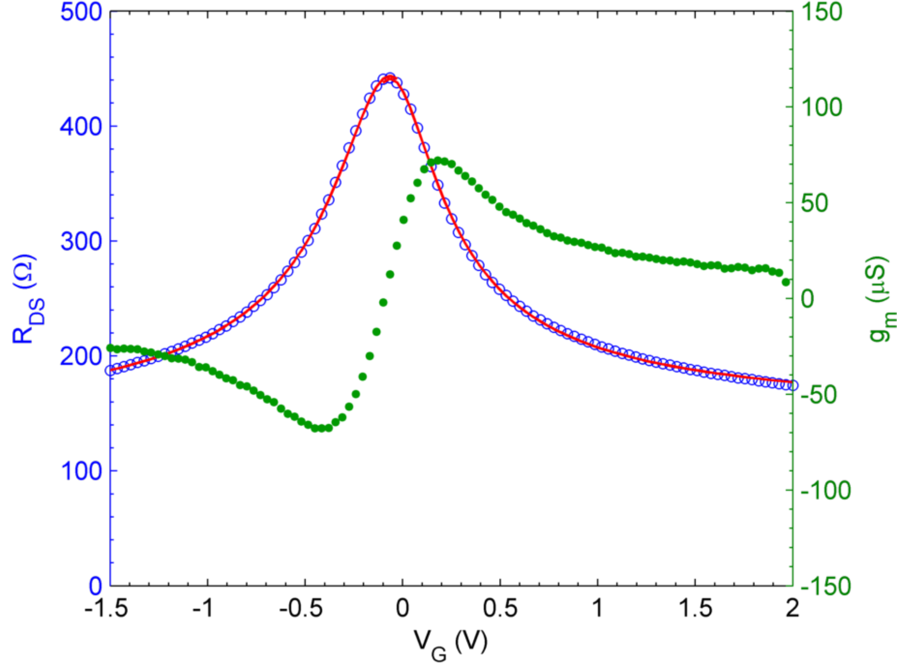

Figure 4.3: Model fit (in red) to source-drain resistance data of a finger-design device with gate length 1000 nm.

Table 4.2: Summary of dc parameters for the finger-design devices with $V_{DS} = 100\,\text{mV}$.

Graphene	L_g (nm)	V_{Dirac} (V)	μ_e, μ_h (cm^2/V s)	max. g_m (μS)
CVD	250	−0.69	700, 1200	69
CVD	500	−0.14	1900, 1800	114
CVD	1000	−0.07	2300, 1800	72

4.1.2 Reliability of GFETs

It is a known problem in GFETs that the DC characteristics display hysteresis [47]. This is seen in a gate-voltage shift of the peak resistance depending on the direction, rate, and range of the gate voltage sweep. This hysteresis is believed to arise from changes in the carrier density of the GFET channel caused by either charge transfer (transferring a carrier from the graphene to a substrate charge trap) or capacitive gating (where charged ions between the graphene and the substrate pull opposite charges onto the graphene from the contacts). The more extreme the gate voltage applied, the more pronounced these effects and the larger the hysteresis observed. It is thought that an adsorbed water layer on the graphene and between the graphene and the substrate contributes to hysteresis, and removal of this adsorbate layer by current annealing has been shown to reduce hysteresis in graphene [48]. Some hysteresis was observed in measurements of the GFETs of every design. To reduce the hysteresis as much as possible the gate voltage was swept in a narrow window and at a moderate rate. For consistency when fitting data and making comparisons, the *sweep down* data, from positive to negative

gate voltage, was always selected.

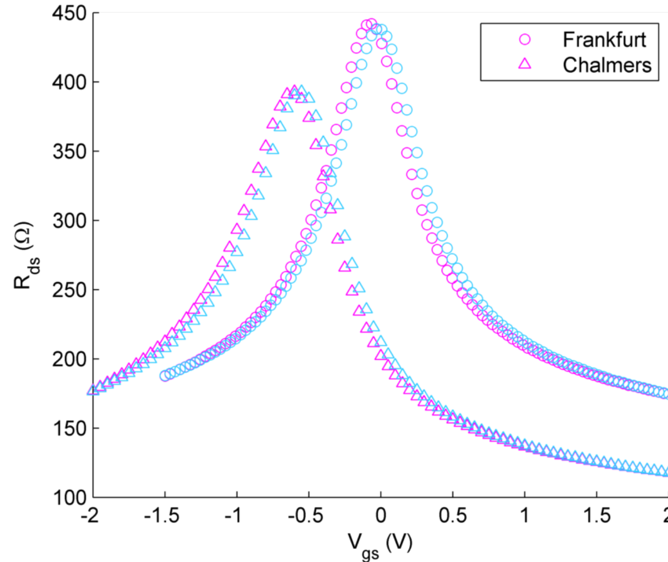

Figure 4.4: Resistance data of a finger-design device with gate length 1000 nm. The triangles represent measurements made at Chalmers, and the circles measurements made in Frankfurt two weeks later. The magenta points are a gate voltage sweep from negative to positive (sweep up) and the blue points are a gate voltage sweep from positive to negative (sweep down).

In addition to the issue of hysteresis, GFETs also suffer from problems with stability over time. The GFETs were first characterized with dc measurements made at Chalmers and then additional dc measurements were made in Frankfurt two weeks later. Between measurements the GFETs were stored in a nitrogen-atmosphere storage box, and still a significant shift in the Dirac voltage was observed in the later measurements. Figure 4.4 is an example of a typical GFET device showing both hysteresis and Dirac voltage shift over time.

The hysteresis and instability of GFETs over time are obstacles that must be overcome in order for GFETs to be more widely used in applications. For the sake of comparison, in this thesis the data considered for all devices is the sweep down data measured in Frankfurt.

4.2 High-frequency measurements

To assess the THz response of the detectors, the devices were individually irradiated with the 0.6 THz beam. A signal was read out at the drain while sweeping the gate voltage in the vicinity of the Dirac voltage.

4.2.1 Optical responsivity

The current response and voltage response were measured for multiple devices of each design. In the interest of brevity, data from one representative device

of each design is presented. From the measured current response R_I and voltage response R_V, the optical responsivity can be calculated using Equations 4.4 (current) and 4.5 (voltage).

$$\Re_I = 2.2\frac{R_I}{P} \tag{4.4}$$

$$\Re_V = 2.2\frac{R_V}{P} \tag{4.5}$$

The factor of 2.2 arises from lock-in detection, because the beam is modulated with a square wave (as opposed to sinusoidal modulation). The beam power P is the measured beam power (290 μW) without taking losses from the silicon lens or the antenna mismatch into account. Additionally, the antenna efficiency and impedance mismatch between the antenna and the device determine how much of the incident radiation is coupled to the GFET. For this split bow-tie antenna design the calculation of antenna efficiency is not straightforward and involves many assumptions. Therefore, the total beam power is used in the calculation to avoid large uncertainties. This means that the responsivity calculated is a minimum value, because not all of the beam power is coupled to the GFET.

The optical current and voltage responsivities for each of the detectors are shown in Figures 4.5, 4.6, 4.7, 4.8, 4.9, and 4.10. Qualitatively, the shapes of the responsivities match those of the transconductance calculated from DC measurements. As wth the transconductance, the responsivities go through zero and change sign near the Dirac voltage.

While the magnitude of the transconductance maxima and minima are similar, the magnitude of the responsivity maxima and minima are not. It is expected that the responsivity will be symmetric (although with opposite sign) around the Dirac voltage since the electron and hole branches of the DC resistance data are nearly symmetric. However, the resposivity maximum at more positive gate voltages is always larger than the magnitude of the responsivity minimum, indicating a systematic shift in the measured response. Thermal effects can be ruled out as causing this shift because it was present independent ofl modulation frequency in the range 33 Hz–3.3 kHz, but without a more in-depth physical treament of the results it is difficult to identify the cause of the shift.

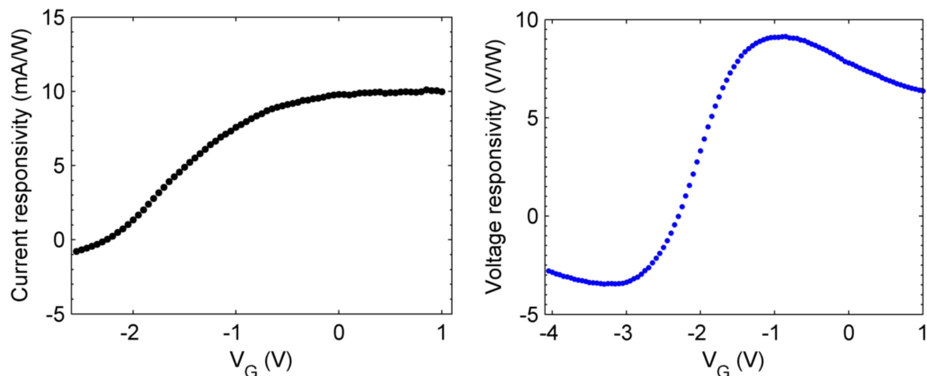

Figure 4.5: Current and voltage responsivity of the exfoliated graphene detector, $W_g = 2\,\mu$m.

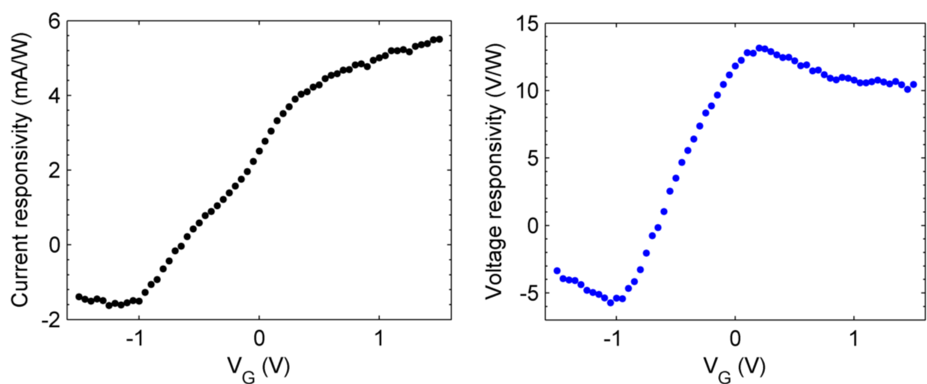

Figure 4.6: Current and voltage responsivity of a CVD graphene detector, $W_g = 2\,\mu$m.

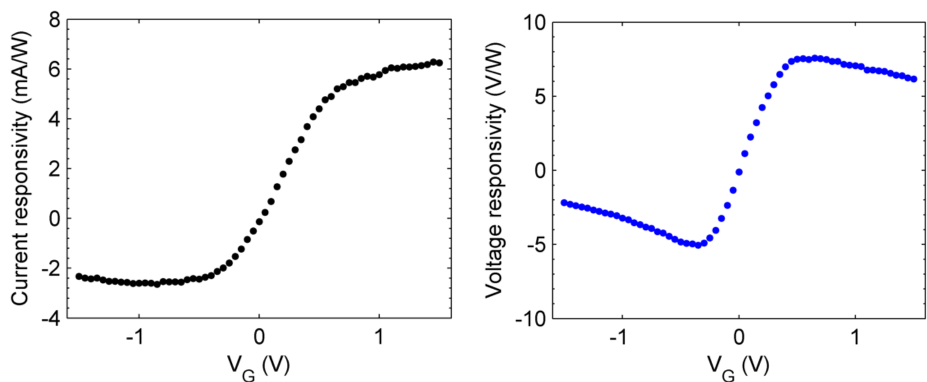

Figure 4.7: Current and voltage responsivity of a CVD graphene detector, $W_g = 5\,\mu$m.

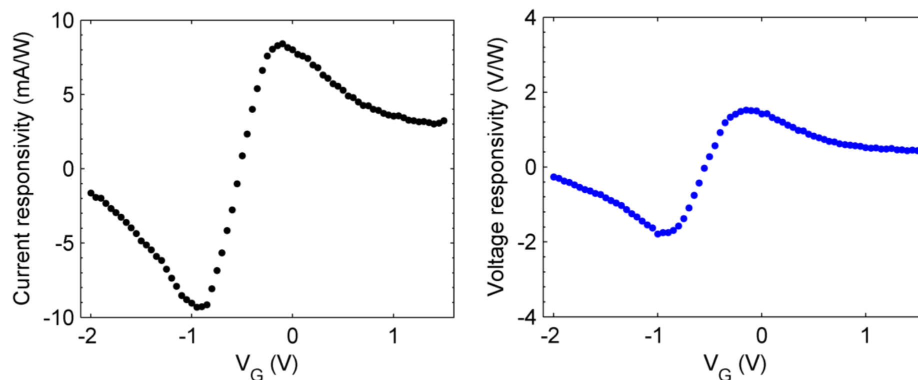

Figure 4.8: Current and voltage responsivity of a CVD graphene detector, $L_g = 250\,\text{nm}$.

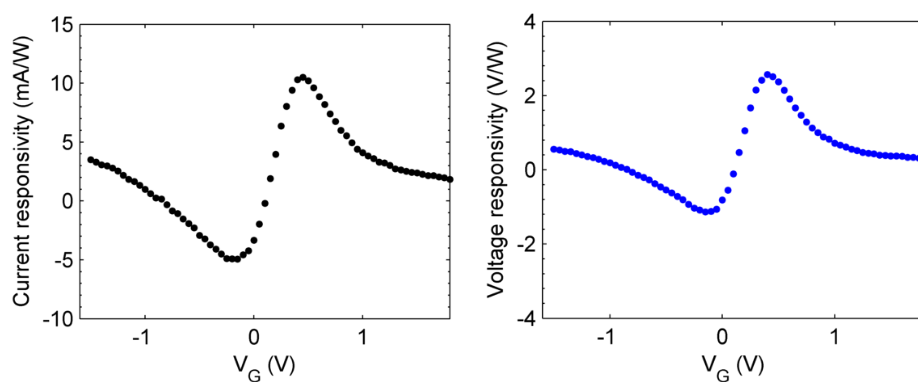

Figure 4.9: Current and voltage responsivity of a CVD graphene detector, $L_g = 500\,\text{nm}$.

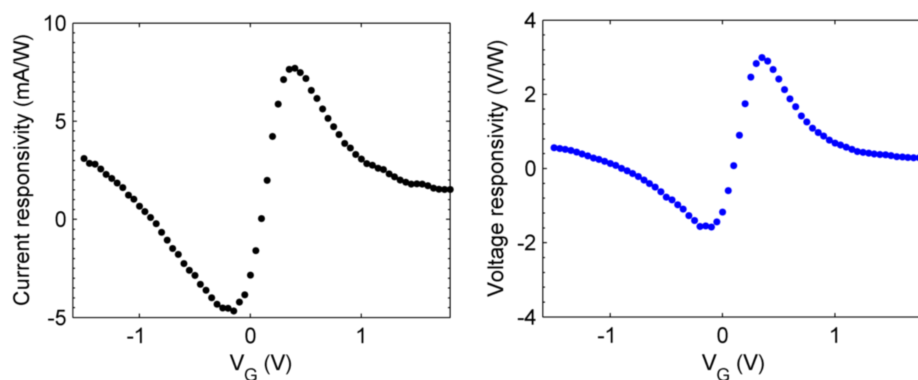

Figure 4.10: Current and voltage responsivity of a CVD graphene detector, $L_g = 1000\,\text{nm}$.

4.2.2 Noise-equivalent power

In order to compare the sensitivity of direct detectors, the relevant figure-of-merit is the noise-equivalent power (NEP). NEP is defined as the signal power that gives a signal-to-noise ratio of 1 in a 1 Hz output bandwidth. Practially speaking, a smaller NEP means a more sensitive detector, as a smaller signal power can be detected. In this thesis, NEP refers to the optical NEP, that is, it refers to the incident power on the detector. In the calculation of NEP, we assume only thermal voltage noise in our detector, given by Equation 4.6 [49, 50].

$$N = \sqrt{4k_B T R_{DS}} \tag{4.6}$$

In the noise calculation, k_B is Boltzmann's constant, T is temperature, and R_{DS} is the drain-source resistance. The assumption of thermal noise is valid for zero drain bias and a very small gate leakage current, which was measured to be less than 1 nA for the detectors. Measurements were made at room temperature and the drain-source resistance was taken as the ratio between the voltage and current responsivities.

The NEP is the ratio of the noise to the responsivity, shown in Equation 4.7. Although both current and voltage responsivities were calculated, the NEP values presented were all calculated from the voltage responsivity data.

$$\text{NEP} = \frac{N}{\Re_V} = \frac{\sqrt{4k_B T R_{DS}}}{\Re_V} \tag{4.7}$$

For each detector, the NEP was plotted as a function of gate voltage. Figures 4.11, 4.12, 4.13, 4.14, 4.15, and 4.16 show the dependence of NEP on gate voltage. The NEP diverges near the Dirac voltage, because at this voltage the voltage responsivity $\Re_V$ is zero. The plots of NEP for the finger-design detectors (Figures 4.15 and 4.16 diverge for two values of gate voltage because the responsivity changes sign twice.

The values calculated from measurements at 0.6 THz are summarized in Table 4.3, for the same devices that were characterized with DC measurements (parameters given in Tables 4.1 and 4.2). Based on the dc measurements, it should be predicted that the detectors with the highest transconductance would give the highest voltage responsivity, since these have been shown to be qualitatively proportional [44]. However, it is not only the transconductance which is an important parameter but also the overall resistance value R_{DS}. When comparing the detectors within each design, the simple-design detector with $W_g = 2\,\mu$m and the finger-design detector with $L_g = 1000$ nm both have intermediate transconductance, the largest overall drain-source resistance, and interestingly the largest voltage responsivity. While the device transconductance is important, the devices with the largest change in drain-source resistance (the largest difference between minimum and maximum R_{DS}) are those that show the best voltage responsivity. This must mean that although both transconductance and drain-source resistance play a role in predicting the responsivity, the drain-source resistance dominates.

When analyzing the NEP of the different devices, it is not only the voltage responsivity which is important. Those detectors with low drain-source resistance

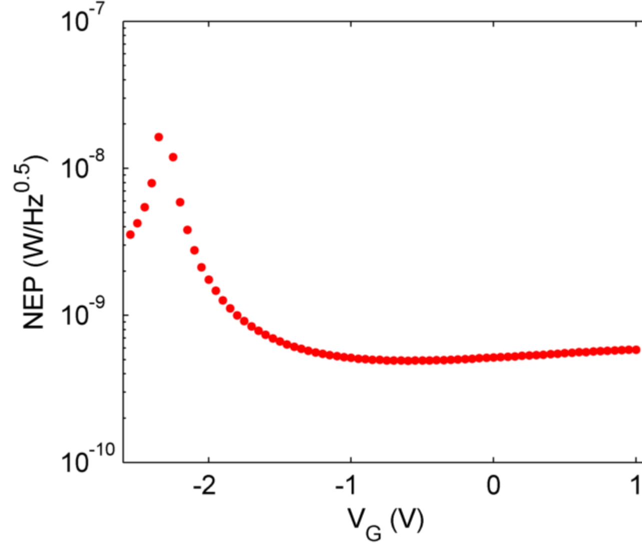

Figure 4.11: NEP of exfoliated graphene detector, $W_g = 2\,\mu$m.

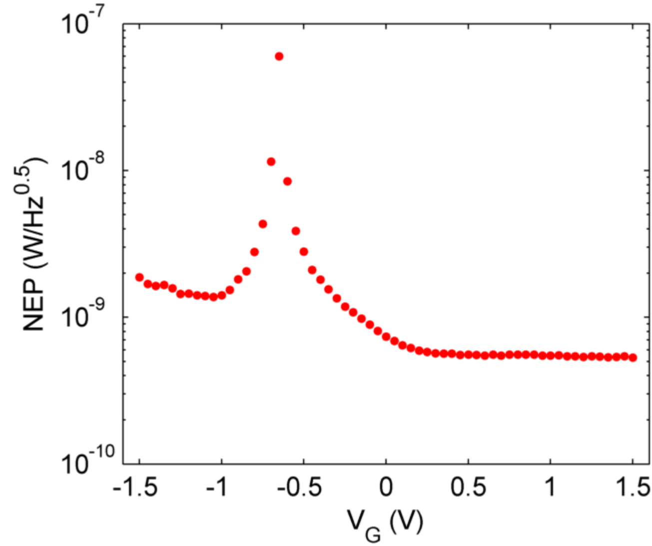

Figure 4.12: NEP of CVD graphene detector, $W_g = 2\,\mu$m.

Table 4.3: Summary of responsivities and NEP for the simple- and finger-design detectors calculated from measurements taken at 0.6 THz.

Device		max. $\Re_V$ (V/W)	max. $\Re_I$ (mA/W)	min. NEP (pW/Hz$^{0.5}$)
$W_g =$	$2\,\mu$m	13.0	5.6	530
CVD	$5\,\mu$m	8.7	6.3	590
exfoliated	$2\,\mu$m	9.1	8.2	490
$L_g =$	250 nm	1.9	10.1	810
	500 nm	2.6	10.5	710
	1000 nm	3.0	7.7	840

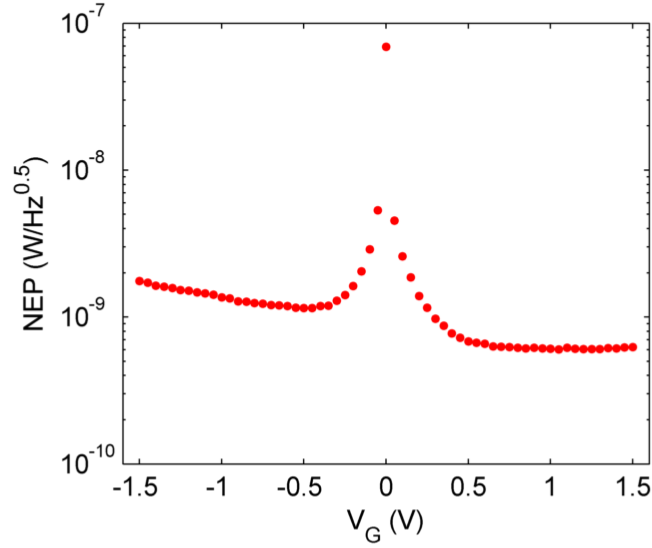

Figure 4.13: NEP of CVD graphene detector, $W_g = 5\,\mu\text{m}$.

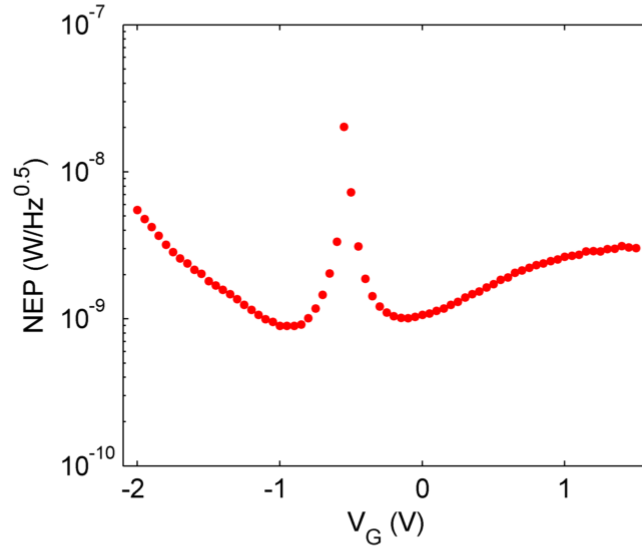

Figure 4.14: NEP of CVD graphene detector, $L_g = 250\,\text{nm}$.

have lower noise, which is as important in decreasing the NEP as having a high voltage responsivity. The simple-design detector made of exfoliated graphene has a lower voltage responsivity than the same detector design made of CVD graphene, but also a much lower drain-source resistance, which results in a lower NEP. This same argument can be made when comparing the finger-design detectors. The detector with a gate length of 500 nm does not have the highest responsivity, but it also does not have the highest drain-source resistance. To have a low NEP, it is necessary to have a high responsivity and a low drain-source resistance. However, as the responsivity results show, the detectors with the lowest drain-source resistance do not have the highest responsivities. It is therefore a balance between drain-source resistance and voltage responsivity that produces the lowest NEP.

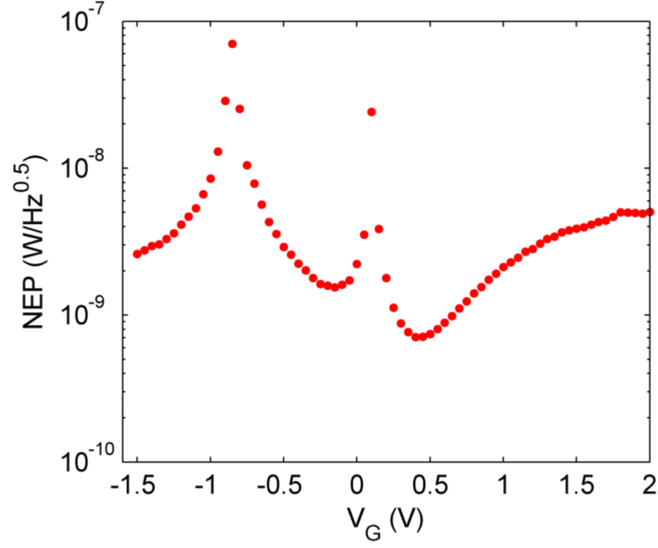

Figure 4.15: NEP of CVD graphene detector, $L_g = 500\,\text{nm}$.

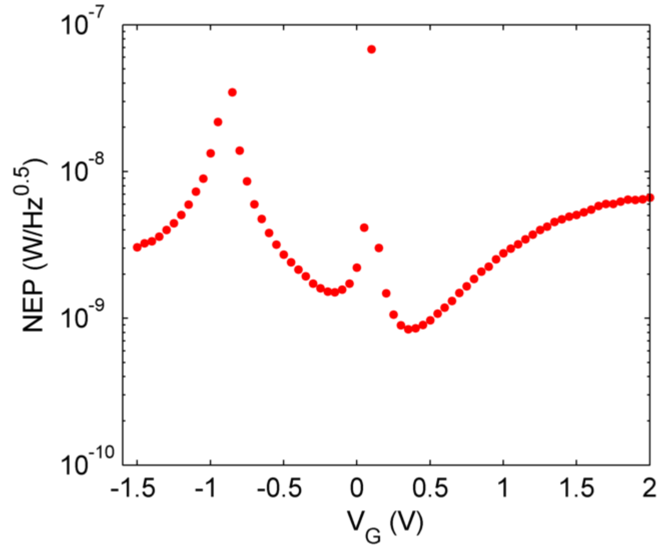

Figure 4.16: NEP of CVD graphene detector, $L_g = 1000\,\text{nm}$.

In the calculation of the responsivity as well as the NEP, the total beam power was used. The consequence is that the NEP values are upper bounds; if the power in the responsivity equation was corrected for losses and antenna coupling efficiency, the responsivity would increase and the NEP would decrease. Still, the NEP values obtained are a signifcant improvement over previous reported values for single-layer graphene of $\sim$200 nW/Hz$^{0.5}$ [14] and bilayer graphene of $\sim$2000 pW/Hz$^{0.5}$ [16]. With NEPs as low as 490 pW/Hz$^{0.5}$ and 530 pW/Hz$^{0.5}$ for the 2 μm-gate-width detectors on exfoliated and CVD graphene, respectively, our detectors are competitive with other room-temperature direct detection technologies, summarized in Table 4.4.

Simulations predicted that the finger design would give better results when measured at 0.6 THz, especially for the 250 nm-gate length. However, this is not

Table 4.4: Comparison of minimum NEP for various room-temperature detector technologies at frequencies near 0.6 THz. The CVD graphene NEP cited is that for the CVD detector with a gate width of 2 μm.

Detector	Minimum NEP (pW/Hz$^{0.5}$)	Source
CVD graphene	530	*this thesis*
Si MOSFET	300	[11]
GaN HEMT	490	[43]
YBCO bolometer	200	[19]
Schottky diode	20–30	[17, 18]
Bilayer graphene FET	~2000	[16]

the case. The reasons for this discrepancy could be numerous, but it is most likely due to an impedance mismatch between the antenna and the GFET. When the antenna characteristics were simulated, the device impedance was taken to be 50 Ω. However, the drain-source resistance measured was instead on the level of kΩ, orders of magnitude higher than the simulation considered. While it seems that the finger detectors, which have a lower device impedance, would be better matched to the antenna, the antenna is capacitive, meaning that the imaginary part of the antenna impedance is large. When describing the impedance of the GFET devices, it is assumed that the impedance has only a real component which is equal to the drain-source resistance, since the drain-source bias was zero. This means that although the GFET impedance of the finger devices is close to the 100 Ω real antenna impedance, the large imaginary part of the antenna impedance causes the mismatch. Therefore, it is the simple-design GFETs with higher R_{DS} which better match the antenna, and this is reflected in the higher responsivities and lower NEPs measured for these detectors.

4.2.3 Beam profile

Although the calculation of the actual incident radiation coupled to the GFET is difficult, the focus of the beam on the antenna can be easily determined. By measuring the current response while stepping the detector in x and y, the beam profile can be calculated. Figure 4.17 shows the current response at various positions x and y relative to the position of the detector at the highest current response.

A Gaussian fit is made to the data, verifying our assumption of a Gaussian beam. By taking the full width at half-maximum of the Gaussian fit, the spot size of the beam can be approximated. This assumes that the beam is focused such that it is perpendicular to the device and that the origin (at 0 mm in x and 0 mm in y) is in the center of the beam spot. The beam is therefore an ellipse with a major axis of 0.2 mm and a minor axis of 0.1 mm. This spot size is confirmation that the beam was well-focused during measurement and completely intercepted by the antenna.

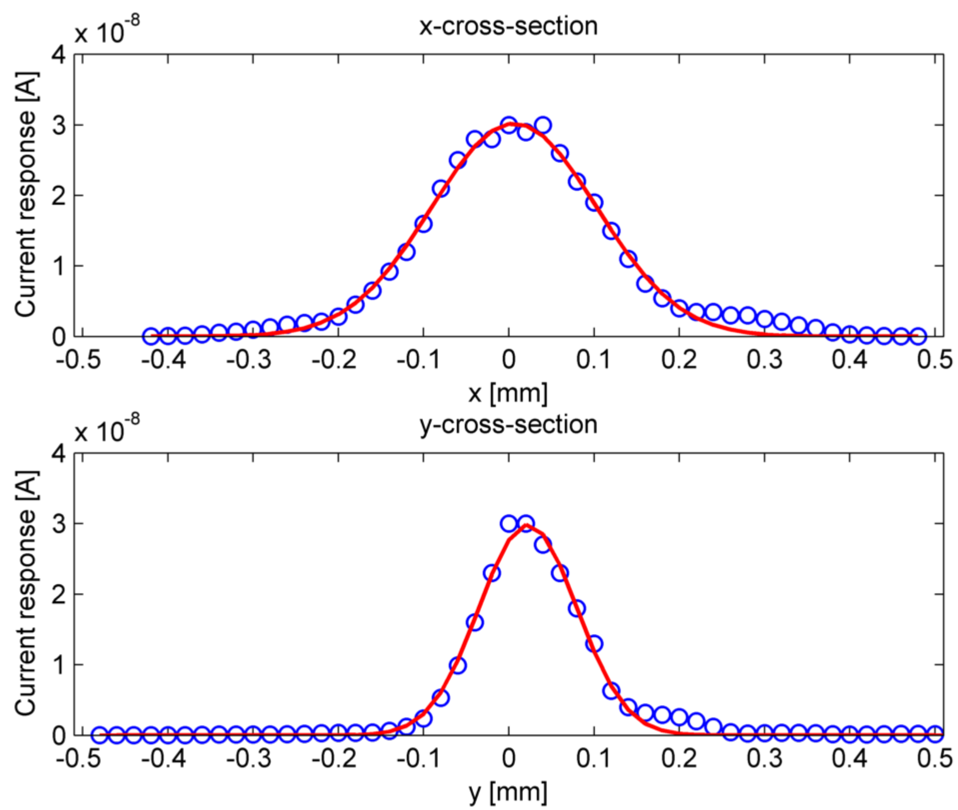

Figure 4.17: Beam profile with Gaussian fit.

5

Conclusions

This thesis demonstrates the first successful room-temperature detection at 0.6 THz using graphene detectors fabricated with both CVD-grown or exfoliated graphene. Record-low NEP values were achieved for CVD- and exfoliated-graphene detectors, and these values are conservative estimates of the NEP. Through the integration of the GFETs with a split bow-tie antenna and more efficient channel modulation, the responsivity of the detectors was greatly improved over previous studies [14, 16]. Two transistor designs were studied in an effort to examine the effect of channel impedance on responsivity. While the finger design had a higher transconductance and therefore should have had a higher responsivity, the capacitive nature of the antenna resulted in a high imaginary antenna impedance, which meant that the resistance in the device was too low to properly match the antenna impedance. The simple design was better matched with the antenna and therefore the THz radiation was better coupled to the graphene channel, resulting in a higher responsivity and lower NEP. While previous work with graphene detectors used exfoliated graphene, in this thesis both exfoliated and CVD graphene are demonstrated to be capable of sensitive, room-temperature detection. As CVD graphene fabrication processes continue to improve, increasingly large-area, high-quality, single-layer graphene can be easily grown. This creates the possibility for scale-up of THz detector production.

5.1 Future work

While the results obtained in this thesis represent a significant improvement in broadband, room-temperature direct detection using graphene, there are a number of ways that these results could be further improved. The coupling of the radiation to the device could be improved by matching the antenna impedance to the device impedance. A wide device with a more ideal antenna could accomplish this aim: the device would have a higher transconductance and if the gate length is short it could have a drain-source resistance (device impedance) closer to the antenna impedance. This would lead to a higher responsivity and lower noise figure, which would mean a more sensitive detector.

Broadband detection of THz radiation has now been demonstrated in a wide variety of materials, but resonant detection at room temperature has yet to be successful. From a physics perspective, resonant detection in graphene detectors could be possible at THz frequencies if the mobility of the graphene could be improved. SiO_2 is not an ideal substrate for graphene as surface phonons and charged impurities strongly reduce graphene mobility, but the advantage of SiO_2 is its prevalence in CMOS processing. Improving the mobility of graphene has been proposed through current annealing [23, 48] to remove impurities from the graphene as well as using a more favorable substrate. Graphene and hexagonal-boron nitride have similar lattice constants, which has resulted in mobilities as high as 25,000 $\mathrm{cm^2/V\,s}$ in graphene on boron nitride [25]. Another alternative has been to avoid the substrate-interaction problem altogether by suspending the graphene above the substrate surface [26, 51] although this poses problems from a processing standpoint. If the predicted mobility of graphene could be realized in a GFET at room temperature, the elusive goal of resonant detection could be achieved. Another route to resonant detection is to measure at higher frequencies. Although sources at these frequencies are limited, if the frequency of incident radiation were increased the mobility requirements could be relaxed.

Measuring responsivity and calculating NEP is important to characterize a detector, but to see a complete picture noise measurements must also be made. In this thesis, thermal noise is assumed to be the dominant noise mechanism, but this is not always the case. The noise parameters of graphene detectors have not been investigated and could give insight into the ultimate sensitivity that is possible with these devices. At low frequencies, the noise is expected to be dominated by $1/f$ noise, which is not seen at the THz frequencies used for measurement.

Bibliography

[1] KS Novoselov, AK Geim, SV Morozov, D Jiang, Y Zhang, SV Dubonos, IV Grigorieva, and AA Firsov. Electric field effect in atomically thin carbon films. *Science*, 306(5696):666–669, OCT 22 2004.

[2] A. K. Geim and K. S. Novoselov. The rise of graphene. *Nature Materials*, 6(3):183–191, MAR 2007.

[3] PH Siegel. Terahertz technology. *IEEE Transactions on Microwave Theory and Techniques*, 50(3):910–928, MAR 2002.

[4] MC Kemp, PF Taday, BE Cole, JA Cluff, AJ Fitzgerald, and WR Tribe. Security applications of terahertz technology. In Hwu, RJ and Woodlard, DL, editor, *Terahertz for Military and Security Applications*, volume 5070 of *Proceedings of the Society of Photo-optical Instrumentation Engineers (SPIE)*, pages 44–52, 2003. Conference on Terahertz for Military and Security Applications, ORLANDO, FL, APR 21, 2003.

[5] JF Federici, B Schulkin, F Huang, D Gary, R Barat, F Oliveira, and D Zimdars. THz imaging and sensing for security applications - explosives, weapons and drugs. *Semiconductor Science and Technology*, 20(7):S266–S280, JUL 2005.

[6] Roger Appleby and H. Bruce Wallace. Standoff detection of weapons and contraband in the 100 GHz to 1 THz region. *IEEE Transactions on Antennas and Propagation*, 55(11, 1):2944–2956, NOV 2007.

[7] PH Siegel. Terahertz technology in biology and medicine. *IEEE Transactions on Microwave Theory and Techniques*, 52(10):2438–2447, OCT 2004.

[8] RM Woodward, VP Wallace, DD Arnone, EH Linfield, and M Pepper. Terahertz pulsed imaging of skin cancer in the time and frequency domain. *Journal of Biological Physics*, 29(2-3):257–261, 2003.

[9] Lena Oehrstroem, Andreas Bitzer, Markus Walther, and Frank Jakobus Ruehli. Technical Note: Terahertz Imaging of Ancient Mummies and Bone. *American Journal of Physical Anthropology*, 142(3):497–500, JUL 2010.

[10] Taiichi Otsuji, Stephane Albon Boubanga Tombet, Akira Satou, Hirokazu Fukidome, Maki Suemitsu, Eiichi Sano, Vyacheslav Popov, Maxim Ryzhii, and Victor Ryzhii. Graphene materials and devices in terahertz science and technology. *MRS Bulletin*, 37(12):1235–1243, DEC 2012.

[11] Alvydas Lisauskas, Ullrich Pfeiffer, Erik Öjefors, Peter Haring Bolivar, Diana Glaab, and Hartmut G. Roskos. Rational design of high-responsivity detectors of terahertz radiation based on distributed self-mixing in silicon field-effect transistors. *Journal of Applied Physics*, 105(11), JUN 1 2009.

[12] Erik Öjefors, Ullrich R. Pfeiffer, Alvydas Lisauskas, and Hartmut G. Roskos. A 0.65 THz Focal-Plane Array in a Quarter-Micron CMOS Process Technology. *IEEE Journal of Solid-state Circuits*, 44(7):1968–1976, JUL 2009. 34th European Solid-State Circuits Conference, Edinburgh, SCOTLAND, SEP 15-19, 2008.

[13] Sebastian Boppel, Alvydas Lisauskas, Martin Mundt, Dalius Seliuta, Linas Minkevicius, Irmantas Kasalynas, Gintaras Valusis, Martin Mittendorff, Stephan Winnerl, Viktor Krozer, and Hartmut G. Roskos. CMOS Integrated Antenna-Coupled Field-Effect Transistors for the Detection of Radiation From 0.2 to 4.3 THz. *IEEE Transactions on Microwave Theory and Techniques*, 60(12, 1):3834–3843, DEC 2012.

[14] L. Vicarelli, M. S. Vitiello, D. Coquillat, A. Lombardo, A. C. Ferrari, W. Knap, M. Polini, V. Pellegrini, and A. Tredicucci. Graphene field-effect transistors as room-temperature terahertz detectors. *Nature Materials*, 11(10):865–871, OCT 2012.

[15] J. S. Moon, H. C. Seo, M. Antcliffe, S. Lin, C. McGuire, D. Le, L. O. Nyakiti, D. K. Gaskill, P. M. Campbell, K. M. Lee, and P. Asbeck. Graphene FET-Based Zero-Bias RF to Millimeter-Wave Detection. *IEEE Electron Device Letters*, 33(10):1357–1359, OCT 2012.

[16] Davide Spirito, Dominique Coquillat, Sergio L. De Bonis, Antonio Lombardo, Matteo Bruna, Andrea C. Ferrari, Vittorio Pellegrini, Alessandro Tredicucci, Wojciech Knap, and Miriam S. Vitiello. High performance bilayer-graphene terahertz detectors. *Applied Physics Letters*, 104(6), FEB 10 2014.

[17] Lei Liu, Jeffrey L. Hesler, Haiyong Xu, Arthur W. Lichtenberger, and Robert M. Weikle, II. A Broadband Quasi-Optical Terahertz Detector Utilizing a Zero Bias Schottky Diode. *IEEE Microwave and Wireless Components Letters*, 20(9):504–506, SEP 2010.

[18] Daniel Schoenherr, Colin Bleasdale, Thorsten Goebel, Cezary Sydlo, Hans L. Hartnagel, Roger Lewis, and Peter Meissner. Extremely Broadband Characterization of a Schottky Diode Based THz Detector. In *35th International Conference on Infrared, Millimeter, and Terahertz Waves (IRMMW-THZ 2010)*, 2010. 35th International Conference on Infrared, Millimeter and Terahertz Waves, Rome, ITALY, SEP 05-10, 2010.

[19] S. Bevilacqua and S. Cherednichenko. Fast room temperature thz bolometers. In *Infrared, Millimeter, and Terahertz Waves (IRMMW-THz), 2013 38th International Conference on*, pages 1–2, Sept 2013.

[20] PR Wallace. The Band Theory of Graphite. *Physical Review*, 71(9):622–634, 1947.

[21] A. H. Castro Neto, F. Guinea, N. M. R. Peres, K. S. Novoselov, and A. K. Geim. The electronic properties of graphene. *Reviews of Modern Physics*, 81(1):109–162, JAN-MAR 2009.

[22] Shaffique Adam, E. H. Hwang, V. M. Galitski, and S. Das Sarma. A self-consistent theory for graphene transport. *Proceedings of the National Academy of Sciences of the United States of America* , 104(47):18392–18397, NOV 20 2007.

[23] Yung-Chang Lin, Chun-Chieh Lu, Chao-Huei Yeh, Chuanhong Jin, Kazu Suenaga, and Po-Wen Chiu. Graphene annealing: How clean can it be? *Nano Letters*, 12(1):414–419, 2012.

[24] X. Li, E. A. Barry, J. M. Zavada, M. Buongiorno Nardelli, and K. W. Kim. Surface polar phonon dominated electron transport in graphene. *Applied Physics Letters*, 97(23), DEC 6 2010.

[25] C. R. Dean, A. F. Young, I. Meric, C. Lee, L. Wang, S. Sorgenfrei, K. Watanabe, T. Taniguchi, P. Kim, K. L. Shepard, and J. Hone. Boron nitride substrates for high-quality graphene electronics. *Nature Nanotechnology*, 5(10):722–726, OCT 2010.

[26] Jannik C. Meyer, A. K. Geim, M. I. Katsnelson, K. S. Novoselov, T. J. Booth, and S. Roth. The structure of suspended graphene sheets. *Nature*, 446(7131):60–63, MAR 1 2007.

[27] P. Blake, E. W. Hill, A. H. Castro Neto, K. S. Novoselov, D. Jiang, R. Yang, T. J. Booth, and A. K. Geim. Making graphene visible. *Applied Physics Letters*, 91(6), AUG 6 2007.

[28] Yanqing Wu, Keith A. Jenkins, Alberto Valdes-Garcia, Damon B. Farmer, Yu Zhu, Ageeth A. Bol, Christos Dimitrakopoulos, Wenjuan Zhu, Fengnian Xia, Phaedon Avouris, and Yu-Ming Lin. State-of-the-Art Graphene High-Frequency Electronics. *Nano Letters*, 12(6):3062–3067, JUN 2012.

[29] M. Tanzid, M. A. Andersson, J. Sun, and J. Stake. Microwave noise characterization of graphene field effect transistors. *Applied Physics Letters*, 104(1), JAN 6 2014.

[30] M. A. Andersson, A. Vorobiev, J. Sun, A. Yurgens, S. Gevorgian, and J. Stake. Microwave characterization of Ti/Au-graphene contacts. *Applied Physics Letters*, 103(17), OCT 21 2013.

[31] Frank Schwierz. Electronics Industry-compatible graphene transistors. *Nature*, 472(7341):41–42, APR 7 2011.

[32] David M Pozar. *Microwave and RF Design of Wireless Systems*. John Wiley & Sons, 2001.

[33] M Dyakonov and M Shur. Detection, mixing, and frequency multiplication of terahertz radiation by two-dimensional electronic fluid. *IEEE Transactions on Electron Devices*, 43(3):380–387, MAR 1996.

[34] M Dyakonov and M Shur. Shallow-water analogy for a ballistic field-effect transistor: New mechanism of plasma-wave generation by dc current. *Physical Review Letters*, 71(15):2465–2468, OCT 11 1993.

[35] Wojciech Knap, Mikhail Dyakonov, Dominique Coquillat, Frederic Teppe, Nina Dyakonova, Jerzy Lausakowski, Krzysztof Karpierz, Maciej Sakowicz, Gintaras Valusis, Dalius Seliuta, Irmantas Kasalynas, Abdelouahad El Fatimy, Y. M. Meziani, and Taiichi Otsuji. Field Effect Transistors for Terahertz Detection: Physics and First Imaging Applications. *Journal of Infrared Millimeter and Terahertz Waves*, 30(12):1319–1337, DEC 2009. 33rd International Conference on Infrared, Millimeter, and Terahertz Waves, Pasadena, CA, SEP, 2008.

[36] W Knap, F Teppe, Y Meziani, N Dyakonova, J Lusakowski, F Boeuf, T Skotnicki, D Maude, S Rumyantsev, and MS Shur. Plasma wave detection of sub-terahertz and terahertz radiation by silicon field-effect transistors. *Applied Physics Letters*, 85(4):675–677, JUL 26 2004.

[37] F Teppe, W Knap, D Veksler, MS Shur, AP Dmitriev, VY Kachorovskii, and S Rumyantsev. Room-temperature plasma waves resonant detection of sub-terahertz radiation by nanometer field-effect transistor. *Applied Physics Letters*, 87(5), AUG 1 2005.

[38] Claire Berger, Zhimin Song, Xuebin Li, Xiaosong Wu, Nate Brown, Cecile Naud, Didier Mayou, Tianbo Li, Joanna Hass, Atexei N. Marchenkov, Edward H. Conrad, Phillip N. First, and Wait A. de Heer. Electronic confinement and coherence in patterned epitaxial graphene. *Science*, 312(5777):1191–1196, MAY 26 2006.

[39] Xuesong Li, Weiwei Cai, Jinho An, Seyoung Kim, Junghyo Nah, Dongxing Yang, Richard Piner, Aruna Velamakanni, Inhwa Jung, Emanuel Tutuc, Sanjay K. Banerjee, Luigi Colombo, and Rodney S. Ruoff. Large-Area Synthesis of High-Quality and Uniform Graphene Films on Copper Foils. *Science*, 324(5932):1312–1314, JUN 5 2009.

[40] Jie Sun, Niclas Lindvall, Matthew T. Cole, Koh T. T. Angel, Teng Wang, Kenneth B. K. Teo, Daniel H. C. Chua, Johan Liu, and August Yurgens. Low Partial Pressure Chemical Vapor Deposition of Graphene on Copper. *IEEE Transactions on Nanotechnology*, 11(2):255–260, MAR 2012.

[41] Cesar J. Lockhart de la Rosa, Jie Sun, Niclas Lindvall, Matthew T. Cole, Youngwoo Nam, Markus Loffler, Eva Olsson, Kenneth B. K. Teo, and August Yurgens. Frame assisted H2O electrolysis induced H-2 bubbling transfer of large area graphene grown by chemical vapor deposition on Cu. *Applied Physics Letters*, 102(2), JAN 14 2013.

[42] A. C. Ferrari, J. C. Meyer, V. Scardaci, C. Casiraghi, M. Lazzeri, F. Mauri, S. Piscanec, D. Jiang, K. S. Novoselov, S. Roth, and A. K. Geim. Raman spectrum of graphene and graphene layers. *Physical Review Letters*, 97(18), NOV 3 2006.

[43] Maris Bauer, Alvydas Lisauskas, Sebastian Boppel, Martin Mundt, Viktor Krozer, Hartmut G. Roskos, Serguei Chevtchenko, Joachim Wuerfl, Wolfgang Heinrich, and Guenther Traenkle. Bow-Tie-Antenna-Coupled Terahertz Detectors using AlGaN/GaN Field-Effect Transistors with 0.25 Micrometer Gate Length. In *2013 8th European Microwave Integrated Circuits Conference (EUMIC)*, pages 212–215, 2013. 8th European Microwave Integrated Circuits Conference (EuMIC), Nuremberg, GERMANY, OCT 06-08, 2013.

[44] M. Sakowicz, M. B. Lifshits, O. A. Klimenko, F. Schuster, D. Coquillat, F. Teppe, and W. Knap. Terahertz responsivity of field effect transistors versus their static channel conductivity and loading effects. *Journal of Applied Physics*, 110(5), SEP 1 2011.

[45] Omid Habibpour, Josip Vukusic, and Jan Stake. A Large-Signal Graphene FET Model. *IEEE Transactions on Electron Devices*, 59(4):968–975, APR 2012.

[46] MD Groner, JW Elam, FH Fabreguette, and SM George. Electrical characterization of thin Al2O3 films grown by atomic layer deposition on silicon and various metal substrates. *Thin Solid Films*, 413(1-2):186–197, JUN 24 2002.

[47] Haomin Wang, Yihong Wu, Chunxiao Cong, Jingzhi Shang, and Ting Yu. Hysteresis of Electronic Transport in Graphene Transistors. *ACS Nano*, 4(12):7221–7228, DEC 2010.

[48] J. Moser, A. Barreiro, and A. Bachtold. Current-induced cleaning of graphene. *Applied Physics Letters*, 91(16), OCT 15 2007.

[49] J. B. Johnson. Thermal agitation of electricity in conductors. *Physical Review*, 32:97–109, Jul 1928.

[50] H. Nyquist. Thermal agitation of electric charge in conductors. *Physical Review*, 32:110–113, Jul 1928.

[51] K. I. Bolotin, K. J. Sikes, J. Hone, H. L. Stormer, and P. Kim. Temperature-dependent transport in suspended graphene. *Physical Review Letters*, 101(9), AUG 29 2008.